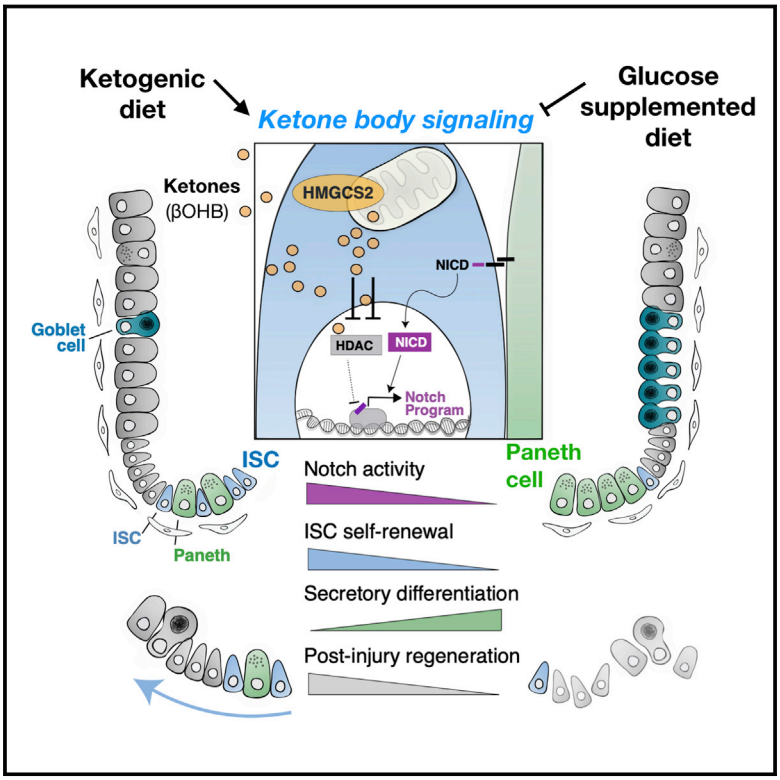
Article

Cell

Ketone Body Signaling Mediates Intestinal Stem Cell Homeostasis and Adaptation to Diet

Graphical Abstract



Authors

Chia-Wei Cheng, Moshe Biton, Adam L. Haber, ..., Maria M. Mihaylova, Aviv Regev, Ömer H. Yilmaz

Correspondence

ohyilmaz@mit.edu

In Brief

Ketone body metabolites inform intestinal stem cell decisions in response to diverse diets.

Highlights

- HMGCS2 enriches for Lgr5^{+} ISCs to generate the ketone body βOHB
- βOHB depletion reduces stemness, alters differentiation, and hampers regeneration
- βOHB, through class I HDAC inhibition, reinforces the NOTCH program in ISCs
- Dietary fat and glucose counter-regulate ketone body signaling to instruct ISCs

Cheng et al., 2019, Cell *178*, 1115–1131
August 22, 2019 © 2019 Elsevier Inc.
https://doi.org/10.1016/j.cell.2019.07.048

CellPress

Cell

Ketone Body Signaling Mediates Intestinal Stem Cell Homeostasis and Adaptation to Diet

Chia-Wei Cheng,[1] Moshe Biton,[5,6,17] Adam L. Haber,[6,17] Nuray Gunduz,[1,13] George Eng,[1,4] Liam T. Gaynor,[8] Surya Tripathi,[1] Gizem Calibasi-Kocal,[1,14] Steffen Rickelt,[1] Vincent L. Butty,[10] Marta Moreno-Serrano,[1] Ameena M. Iqbal,[1] Khristian E. Bauer-Rowe,[1] Shinya Imada,[1,15] Mehmet Sefa Ulutas,[1,16] Constantine Mylonas,[2] Mark T. Whary,[3] Stuart S. Levine,[10] Yasemin Basbinar,[14] Richard O. Hynes,[1,7] Mari Mino-Kenudson,[4] Vikram Deshpande,[4] Laurie A. Boyer,[2] James G. Fox,[3] Christopher Terranova,[11] Kunal Rai,[11] Helen Piwnica-Worms,[12] Maria M. Mihaylova,[9] Aviv Regev,[1,6,7] and Ömer H. Yilmaz[1,2,4,6,18,*]

[1]Koch Institute for Integrative Cancer Research at MIT, Cambridge, MA 02139, USA
[2]Department of Biology, MIT, Cambridge, MA 02139, USA
[3]Division of Comparative Medicine, Department of Biological Engineering, MIT, Cambridge, MA 02139, USA
[4]Department of Pathology, Massachusetts General Hospital Boston and Harvard Medical School, Boston, MA 02114, USA
[5]Department of Molecular Biology, Massachusetts General Hospital, Boston, MA 02114, USA
[6]Klarman Cell Observatory, Broad Institute of Harvard and MIT, Cambridge, MA 02142, USA
[7]Howard Hughes Medical Institute, Department of Biology, MIT, Cambridge, MA 02139, USA
[8]Dana-Farber Cancer Institute, 450 Brookline Avenue, Boston, MA 02215, USA
[9]Department of Biological Chemistry and Pharmacology, The Ohio State University, Columbus, OH 43210 USA
[10]BioMicro Center at MIT, Department of Biology, MIT, Cambridge, MA 02139, USA
[11]Genomic Medicine Department, The University of Texas MD Anderson Cancer Center, Houston, TX 77030, USA
[12]Department of Experimental Radiation Oncology, The University of Texas MD Anderson Cancer Center, Houston, TX 77030, USA
[13]Institute of Materials Science and Nanotechnology, National Nanotechnology Research Center (UNAM), Bilkent University, 06800 Ankara, Turkey
[14]Dokuz Eylul University, Institute of Oncology, Department of Translational Oncology, Izmir, Turkey
[15]Department of Gastroenterological and Transplant Surgery, Graduate School of Biomedical and Health Sciences, Hiroshima University, 1-2-3 Kasumi, Minami-ku, Hiroshima 734-8551, Japan
[16]Department of Biology, Siirt University, Science and Arts Faculty, 56100 Siirt, Turkey
[17]These authors contributed equally
[18]Lead Contact
*Correspondence: ohyilmaz@mit.edu
https://doi.org/10.1016/j.cell.2019.07.048

SUMMARY

Little is known about how metabolites couple tissue-specific stem cell function with physiology. Here we show that, in the mammalian small intestine, the expression of *Hmgcs2* (3-hydroxy-3-methylglutaryl-CoA synthetase 2), the gene encoding the rate-limiting enzyme in the production of ketone bodies, including beta-hydroxybutyrate (βOHB), distinguishes self-renewing *Lgr5*$^+$ stem cells (ISCs) from differentiated cell types. *Hmgcs2* loss depletes βOHB levels in *Lgr5*$^+$ ISCs and skews their differentiation toward secretory cell fates, which can be rescued by exogenous βOHB and class I histone deacetylase (HDAC) inhibitor treatment. Mechanistically, βOHB acts by inhibiting HDACs to reinforce Notch signaling, instructing ISC self-renewal and lineage decisions. Notably, although a high-fat ketogenic diet elevates ISC function and post-injury regeneration through βOHB-mediated Notch signaling, a glucose-supplemented diet has the opposite effects. These findings reveal how control of βOHB-activated signaling in ISCs by diet helps to fine-tune stem cell adaptation in homeostasis and injury.

INTRODUCTION

In the mammalian intestine, actively cycling *Lgr5*$^+$ intestinal stem cells (ISCs) depend on the precise control of intrinsic regulatory programs that include the Wnt, Notch, and Bmp developmental signaling pathways as well as extrinsic cues from their environment to dynamically remodel intestinal composition (Barker et al., 2007; Fre et al., 2005; Mihaylova et al., 2014; Nakada et al., 2011; Qi et al., 2017; van der Flier et al., 2009; Yan et al., 2017). *Lgr5*$^+$ ISCs reside at the bottom of intestinal crypts and are supported by Paneth cells in the small intestine (Sato et al., 2011), deep secretory cells in the colon (Sasaki et al., 2016), and stromal cells throughout the small intestine and colon (Degirmenci et al., 2018; Shoshkes-Carmel et al., 2018), which comprise components of the ISC niche. These ISC niche cells elaborate myriad growth factors and ligands that determine ISC identity in part through modulation of these developmental pathways. In addition to these semi-static epithelial and stromal niche components, migratory immune cell subsets provide

inputs that inform stem cell fate decisions through cytokine signaling based on external signals (Biton et al., 2018; Lindemans et al., 2015).

Although significant progress has been made in deciphering how transcription factors or interactions with the niche exert executive control on *Lgr5*$^+$ ISC identity, recent evidence implicates an emerging role for energetic metabolites and metabolism in this process. For example, the Paneth niche cells provide lactate, an energetic substrate, to promote *Lgr5*$^+$ ISC activity through mitochondrial oxidative phosphorylation (Rodríguez-Colman et al., 2017). Furthermore, low-calorie metabolic states extrinsically control stem cell number and function in calorically restricted dietary regimens through the Paneth cell niche (Igarashi and Guarente, 2016; Yilmaz et al., 2012) and intrinsically engage a fatty acid oxidation metabolic program in ISCs to enhance stemness (Mihaylova et al., 2018). However, more investigation is needed to delineate how changes in the ISC microenvironment interplay with stem cell metabolism to control stemness programs.

Recent studies also indicate that dietary nutrients play an important instructive role in the maintenance of tissues and adult stem cells in diverse tissues (Mihaylova et al., 2014). For example, ascorbic acid (i.e., vitamin C) is an essential dietary nutrient that regulates hematopoietic stem cell function via TET2 enzymes (Agathocleous et al., 2017; Cimmino et al., 2017). In the intestine, low levels of dietary vitamin D compromise the function of *Lgr5*$^+$ ISCs (Peregrina et al., 2015). Furthermore, fatty acid components or their derivatives in high-fat diets (HFDs) enhance ISC function through activation of a peroxisome proliferator-activated receptor (PPAR)-delta program (Beyaz et al., 2016) and high levels of dietary cholesterol through phospholipid remodeling (Wang et al., 2018). Although these examples demonstrate that exogenous nutrients couple diet to adult stem cell activity, little is known about how systemic or stem cell-generated endogenous metabolites that become highly enriched in *Lgr5*$^+$ ISCs coordinate cell fate decisions. Here we interrogate how levels of the ketone body beta-hydroxybutyrate (βOHB) in *Lgr5*$^+$ ISCs govern a diet-responsive metabolite signaling axis that modulates the Notch program to sustain intestinal stemness in homeostasis and regenerative adaptation.

RESULTS

The Ketogenic Enzyme HMGCS2 Is Enriched in Lgr5$^+$ ISCs

To identify the metabolic pathways enriched in ISCs, we analyzed RNA-seq data (Beyaz et al., 2016; Mihaylova et al., 2018) from populations of flow-sorted *Lgr5*-GFP^{hi} ISCs (Sato et al., 2009), *Lgr5*-GFP^{low} progenitors (Sato et al., 2009) and CD24$^+$c-Kit$^+$ Paneth cells(Beyaz et al., 2016; Sato et al., 2011) from *Lgr5-eGFP-IRES-CreERT2* knockin mice (Barker et al., 2007; Data and Code Availability). Because Paneth cells are metabolically distinct from ISCs and progenitors (Rodríguez-Colman et al., 2017), we focused on genes differentially expressed between ISCs and progenitors (filtered by two-group comparison $\rho/\rho max = 5e{-}4$; $p < 0.14$, $q < 0.28$). *3-Hydroxy-3-methylglutaryl-CoA synthase 2* (*Hmgcs2*), the gene encoding the rate-limiting step for ketogenesis (schematic, Figure S1A), was a metabolic enzyme with significant differential expression ($p = 0.002$; $q = 0.046$) between *Lgr5*$^+$ ISCs (GFP^{hi} cells) and progenitors (GFP^{low} cells) (Figure 1A; Table S1), which was also in agreement with the published *Lgr5* ISC signature (Muñoz et al., 2012). Last, re-analysis of single-cell transcriptome data from the small intestine (Haber et al., 2017) demonstrated that 65.7% of *Hmgcs2*-expressing cells were stem cells and 16% were transit-amplifying progenitors, which is similar to the distribution observed for *Lgr5*-expressing cells (Figure 1D).

We verified the enrichment of *Hmgcs2* expression in *Lgr5*$^+$ ISCs at both the mRNA and protein levels by qRT-PCR and immunoblots of flow-sorted ISCs, progenitors, and Paneth cells (Figures S1B and S1C). Single-cell immunoblots also illustrated that HMGCS2-expressing cells (HMGCS2$^+$) were highly enriched in flow-sorted *Lgr5*$^+$ ISCs (77.97%) but less frequent in total intestinal crypt cells (21.17%) (Figure S1D). Moreover, dual in situ hybridization (ISH) and immunohistochemistry (IHC) confirmed the concordance between *Lgr5* and *Hmgcs2* expression in the intestine (Figure 1B). Selectively high HMGCS2 expression in crypt base cells (CBCs) was also observed in the human duodenum (Figure 1C). Expression levels of metabolic genes often fluctuate depending on nutrient availability in diverse dietary regimens (Beyaz et al., 2016; Rodríguez-Colman et al., 2017; Wang et al., 2018; Yilmaz et al., 2012). Notably, unlike the metabolic rate-limiting enzymes of glucose metabolism, the TCA cycle, and fatty acid oxidation, *Hmgcs2* mRNA expression is robustly enriched in *Lgr5*$^+$ ISCs compared with progenitors across a range of physiological states (e.g., fed, fasted, and old age), even in fasting, where it is strongly induced (Figures S1E and S1F), raising the possibility that *Hmgcs2* plays a key role in the maintenance of *Lgr5*$^+$ ISCs.

We next engineered heterozygous *Hmgcs2-lacZ* (i.e., *Hmgcs2*$^{V/+}$) reporter mice (Figures 1E and S1G; STAR Methods) to ascertain whether *Hmgcs2*-expressing (*Hmgcs2*$^+$) crypt cells possessed functional stem cell activity in organoid assays. *Hmgcs2*$^{V/+}$ reporter mice were phenotypically indistinguishable from controls in body mass, causal blood glucose, serum βOHB, small intestine length, and crypt depth (Figures S1H–S1L). Consistent with ISH and IHC for *Hmgcs2* (Figures 1B and 1C), β-galactosidase (lacZ) staining of the small intestine from *Hmgcs2*$^{V/+}$ mice predominantly highlighted CBC cells (Figure 1E). Functionally, using a fluorescein di-β-D-galactopyranoside (FDG) substrate of lacZ, we found that the *Hmgcs2*-lacZ$^+$ fraction of crypt cells possessed nearly all of the organoid-propagating activity compared with the lacZ$^-$ fraction (Figure 1F). This finding, together with the strong co-expression of *Hmgcs2* in *Lgr5*+ ISCs (Figures 1A–1D and S1B–S1D) confirms *Hmgcs2*-expressing crypt cells as functional stem cells.

Loss of *Hmgcs2* Compromises Intestinal Stemness and Regeneration

In addition to validating that *Hmgcs2* marks *Lgr5*$^+$ ISCs, we conditionally ablated *Hmgcs2* in the entire intestine, and specifically in *Lgr5*$^+$ ISCs, to decipher how its loss affects stem cell maintenance. We engineered three separate

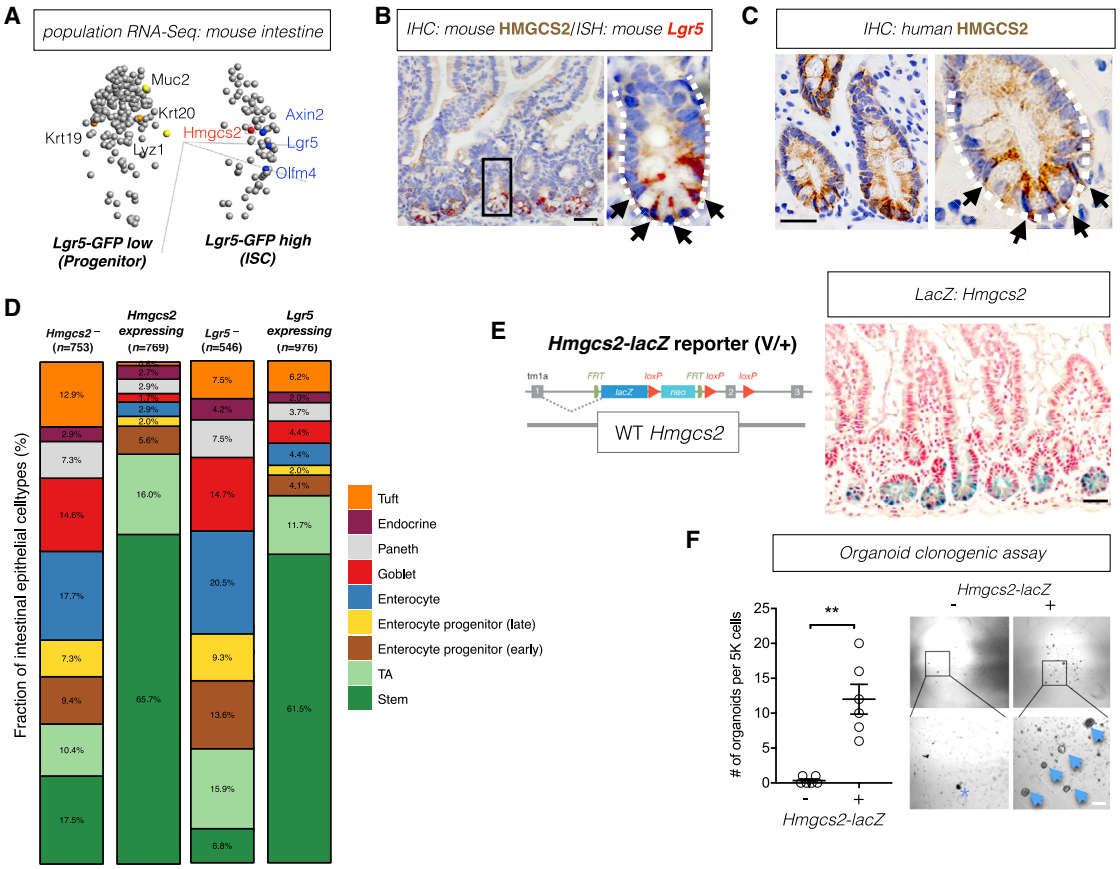


Figure 1. HMGCS2 Enriches for *Lgr5*$^{+}$ Intestinal Stem Cells (ISCs)

(A) Principal-component analysis (PCA) for genes differentially expressed in *Lgr5*-GFP^{low} progenitors versus *Lgr5*-GFP^{hi} ISCs. Variance filtered by (ρ/ρ_{max}) = 5e−4; p = 0.14, *q* = 0.28; plot/total: 253/4,5578 variables. *Axin2*, axin-like protein 2; *Hmgcs2*, 3-hydroxy-3-methylglutaryl-CoA synthase 2; *Lgr5*, leucine-rich repeat-containing G-protein coupled receptor 5; *Olfm4*, Olfactomedin 4; n = 4 mice. See also Table S1.

(B) Mouse HMGCS2 protein expression by immunohistochemistry (IHC, brown) and *Lgr5* expression by in situ hybridization (ISH, red). The white dashed line defines the intestinal crypt, and black arrows indicate HMGCS2^{+} cells. The image represents one of 3 biological replicates. Scale bar, 50 μm.

(C) Human HMGCS2 protein expression by IHC (brown). The white dashed line defines the intestinal crypt, and black arrows indicate HMGCS2^{+} cells. The image represents one of 10 biological replicates. Scale bar, 50 μm.

(D) Stacked barplots show cell composition (percent) of *Hmgcs2*$^{-}$, *Hmgcs2*-expressing, *Lgr5*$^{-}$, and *Lgr5*-expressing intestinal epithelial cells. Numbers in parentheses indicate the total number (n) of the noted cell populations.

(E) *Hmgcs2*-lacZ reporter construct, where the lacZ-tagged allele reflects endogenous *Hmgcs2* expression (left). Also shown is *Hmgcs2*-lacZ expression (blue) in the small intestine (right). The image represents one of 3 biological replicates. Scale bar, 50 μm.

(F) Organoid-forming potential of flow-sorted *Hmgcs2*-lacZ^{-} and *Hmgcs2*-lacZ^{+} crypt epithelial cells (7AAD^{-}EpCAM^{+}). 5,000 cells from each population were flow-sorted into Matrigel with crypt culture medium. Arrows indicate organoids, and the asterisk indicates aborted organoid debris. The numbers of organoids formed from plated cells were quantified at 5 days in culture. Data represent mean ± SEM. **p < 0.01. n = 6 samples from 3 mice. Scale bar, 20 μm.

tamoxifen-inducible conditional alleles (STAR Methods). The first model is the *Hmgcs2*$^{loxp/loxp}$*; Villin-CreERT2* conditional intestinal knockout model, which disrupts *Hmgcs2* in all intestinal epithelial cell types upon tamoxifen administration (Figure 2A; termed iKO). The second model is the *Hmgcs2*$^{loxp/loxp}$*; Lgr5-EGFP-IRES-CreERT2* reporter mouse, where the *Lgr5* knockin allele has mosaic expression in the intestine and permits enumeration and isolation of *Lgr5*-GFP^{hi} ISCs by flow cytometry as well as deletion of *Hmgcs2* in the GFP^{hi} subset of ISCs upon tamoxifen administration (Figures S2A and S2B; termed Lgr5-GFP reporter). This model is often used to quantify GFP^{hi} ISCs and GFP^{low} progenitors (Beyaz et al., 2016; Mihaylova et al., 2018; Sato et al., 2009; Yilmaz et al., 2012). The third model is the *Hmgcs2*$^{loxp/loxp}$*; Lgr5-IRES-CreERT2; Rosa26*$^{LSL\text{-}tdTomato}$ reporter mouse (termed Lgr5 lineage tracer), which enables deletion of *Hmgcs2* upon tamoxifen administration in nearly all *Lgr5*$^{+}$ ISCs and permanent tdTomato labeling of stem cells and their progeny over time (Figures S2D–S2F). Given that this *Lgr5-IRES-CreERT2* allele (Huch et al., 2013) is expressed by nearly all *Lgr5*$^{+}$ ISCs, this third model (similar to the first iKO model) enables quantification of how loss of a gene in ISCs, for example, alters the differentiation of stem cell-derived progeny

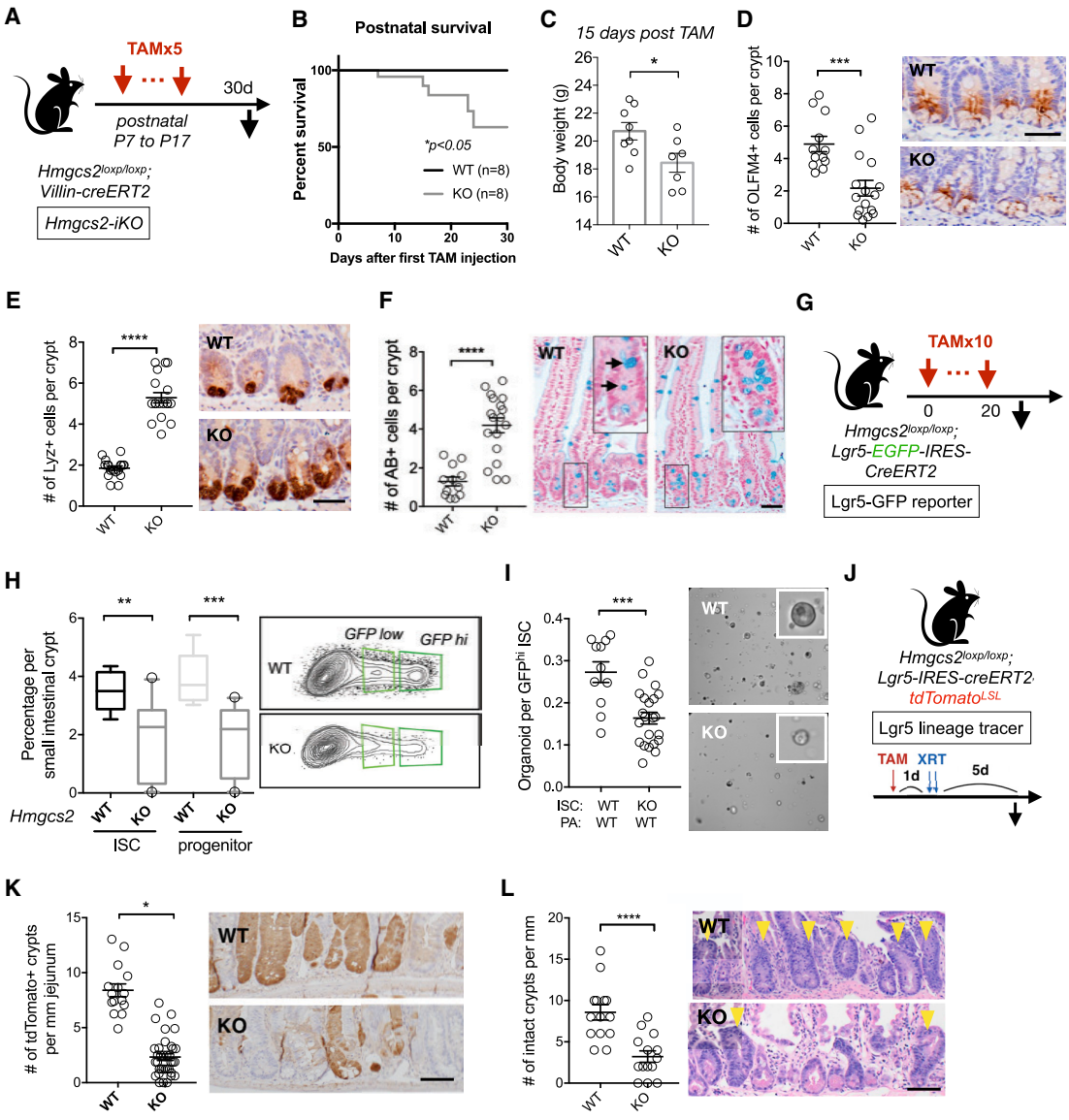


Figure 2. Loss of *Hmgcs2* Compromises ISC Self-Renewal and Differentiation

(A) Schematic of intestinal *Hmgcs2* deletion in postnatal mice with *Villin-CreERT2* (iKO), including the timeline for tamoxifen (TAM) injections and tissue collection.

(B) Kaplan–Meier survival curves of the WT and *Hmgcs2*-iKO mice starting on the first day of tamoxifen injection.

(C) Body weights of WT and *Hmgcs2*-iKO mice 15 days after the first TAM injection.

(D–F) Quantification (left) and representative images (right) of OLFM4^{+} stem cells by IHC (D), lysozyme $^{+}$ (LYZ^{+}) Paneth cells by IHC and (E), Mucin^{+} goblet cells by Alcian blue (AB) (F) in proximal jejunal crypts. n > 5 mice per group. Mice were analyzed at the age of 37 days. Scale bars, 100 μm.

(G) Schematic of Hmgcs2 deletion with *Lgr5-EGFP-IRES-CreERT2* (Lgr5-GFP reporter), including the timeline for TAM injections and tissue collection. 1 day after the last TAM injection (day 21), ISCs and Paneth cells from WT or conditional *Hmgcs2*-null (KO) intestinal crypts were isolated using flow cytometry.

(H) Frequency of 7AAD^{-}/EpCAM^{+}/CD24^{-}/*Lgr5*-GFP^{hi} ISCs and *Lgr5*-GFP^{low} progenitors in crypt cells from WT and KO mice by flow cytometry. n > 10 mice per group.

(I) Organoid-forming assay for sorted *Hmgcs2* WT and KO ISCs co-cultured with WT Paneth cells. Shown are representative images of day 5 organoids. n > 10 mice per group. Scale bar, 100 μm.

(J) Schematic of the Lgr5 lineage tracing, including a timeline of TAM injection, irradiation (XRT, 7.5 Gy × 2) and tissue collection.

(K and L) Quantification and representative images of tdTomato^{+} *Lgr5*$^{+}$ ISC-derived progeny labeled by IHC for tdTomato (K) and number of surviving crypts assessed by microcolony assay (L). Scale bar, 100 μm. n > 25 crypts per measurement, n > 5 measurements per mouse, and n > 3 mice per group.

For box-and-whisker plots (H), the data are expressed as 10–90 percentiles. For dot plots (C–F, I, K, and L), the data are expressed as mean ± SEM. *p < 0.05, **p < 0.01, ***p < 0.005, ****p < 0.001. n > 25 crypts per measurement, n > 3 measurements, per mouse and n > 5 mice per group.

within the entire intestine and also permits fate mapping from *Lgr5*$^{+}$ ISCs (Figure S2M).

In the iKO model, we administered five doses of tamoxifen, starting at post-natal day 7, to iKO and control mice (Figure 2A). Interestingly, intestinal *Hmgcs2* loss reduced the survival of iKO mice where no mortality was noted in the control cohort, and 15 days post-tamoxifen, iKO mice had a modest but significant reduction in body mass relative to controls (Figures 2A–2C). Also, at this same time point, there was a more than 2-fold reduction in the numbers of Olfactomedin 4 (OLFM4)-positive cells, a marker co-expressed by *Lgr5*$^{+}$ ISCs and early progenitors (Figure 2D), and a more than 2-fold increase in the numbers of lysozyme 1 (LYZ1)$^{+}$ Paneth cells and Alcian blue (AB)$^{+}$ goblet cells (Figures 2E and 2F). These findings indicate that *Hmgcs2* plays an essential role in sustaining ISC numbers and lineage-balanced differentiation in the juvenile intestine.

To specifically interrogate the role of *Hmgcs2* in adult ISC maintenance, we ablated *Hmgcs2* in 12-week-old adult *Lgr5*-GFP reporter mice for 3 weeks (Figures 2G, S2A, and S2B), which decreased the frequencies of *Lgr5-GFP*^{hi} ISCs and *Lgr5-GFP*^{low} progenitors by 50% (Figure 2H). When co-cultured with wild-type (WT) Paneth cells, flow-sorted *Hmgcs2*-null ISCs engendered 42.9% fewer and 34.6% smaller organoids compared with WT ISCs, indicating that *Hmgcs2* loss in ISCs cell-autonomously attenuates organoid-initiating capacity (Figures 2I and S2C). Similarly, in *Lgr5*-tdTomato lineage tracer mice, *Hmgcs2* loss gradually reduced the numbers of OLFM4^{+} ISCs with no change in the proliferation or apoptosis of ISCs and progenitors (Figures S2G, S2J, and S2K), small intestine length (Figure S2H), or crypt depth (Figure S2I). As observed in the iKO model, the reduction in the number of OLFM4^{+} ISCs was accompanied by increases in the number of Paneth cells and goblet cells (Figure S2G); however, the numbers of chromogranin A^{+} enteroendocrine cells in the crypts were not affected (Figure S2L). Loss of *Hmgcs2* in adult intestine not only dampens ISC self-renewal (i.e., fewer ISCs with less organoid-forming potential) but also shifts early differentiation within the crypt toward the secretory lineage (i.e., greater numbers of Paneth and goblet cells).

Lgr5^{+} ISCs drive intestinal maintenance in homeostasis and regeneration in response to injury, such as radiation-induced damage (Beumer and Clevers, 2016; Metcalfe et al., 2014). We induced tdTomato expression and *Hmgcs2* excision in *Lgr5*$^{+}$ ISCs with tamoxifen 1 day prior to radiation-induced intestinal epithelial injury to ascertain whether *Hmgcs2* affected the *in vivo* ability of these ISCs to regenerate the intestinal lining (Figure 2J). We assessed the efficiency of regeneration by quantifying the number of tdTomato^{+} clonal progeny generated from the *Lgr5*$^{+}$ ISCs 5 days post-radiation exposure and the number of intact crypt units per length of intestine. First, *Hmgcs2*-null ISCs generated 5-fold fewer labeled tdTomato+ crypts (Figures 2J and 2K) with fewer labeled progeny extending up crypt-villous units, as observed in controls (Figure S2M). Second, loss of *Hmgcs2* also diminished the overall number of surviving intact crypts by 2-fold compared with controls (Figure 2L). Thus, these data demonstrate that *Hmgc2* is critical for *Lgr5*$^{+}$ ISC-mediated repair *in vivo* after injury.

HMGCS2 Regulates Secretory Differentiation through Notch Signaling

To gain mechanistic insight into how *Hmgcs2* affects the differentiation of ISCs, we performed droplet-based scRNA-seq (Figure 3A; STAR Methods) on the sorted tdTomato^{+} progeny of WT and *Hmgcs2*-null ISCs 5 days after tamoxifen injection, a time point prior to the reduction in the number of *Hmgcs2*-null ISCs (Figure S2G Haber et al., 2017), chosen to allow us to capture early changes in regulatory programs. Cell type clustering based on the expression of known marker genes partitioned the crypt cells into seven cell types (Figures 3B, 3C and S3A–S3C; Tables S2 and S3; STAR Methods; Haber et al., 2017).

Acute deletion of *Hmgcs2* in ISCs led to a modest increase in the fraction stem cells (35.34% compared with 22.96% by WT ISCs), fewer transient amplifying/bipotential progenitors (Kim et al., 2016) (transit-amplifying [TA], 18.40% compared with 25.73% by WT ISCs), and a pronounced 5.8-fold expansion of Paneth cells (7.88% compared with 1.36% by WT ISCs) (Figure 3D; Table S2). Further analysis of ISC profiles revealed that, although *Hmgcs2* loss weakened the *Lgr5*$^{+}$ stemness signature (Muñoz et al., 2012) in ISCs (Figure 3E), it had only minor effects on proliferation and apoptosis signatures (Figures S3E and S3F). Together with the progressive loss of ISCs and the shift toward Paneth and goblet cell differentiation observed at later time points after induction of *Hmgcs2* deletion (Figures 2D–2F, 2H and S2G these data support the notion that *Hmgcs2* loss compromises stemness and skews their differentiation toward the secretory lineage.

These findings prompted us to investigate for signs of premature differentiation in *Hmgcs2*-null ISCs, which, surprisingly, show upregulation of Paneth cell signature genes (Figure 3F). Although, 6 days after *Hmgcs2* loss in ISCs, there was no effect on the numbers of tdTomato^{+} stem cells (*Lgr5*-GFP^{hi}) or progenitors (*Lgr5*-GFP^{low}) (Figure S3H), *Hmgcs2*-null ISCs engendered substantially greater numbers of tdTomato^{+} Paneth cells after as few as 24 h of deletion in jejunal sections (Figures 3G and S3G) and after 6 days of deletion by flow cytometry (Figure S3H).

In the mammalian intestine, Notch signaling activates *Olfm4* transcription (a co-marker for *Lgr5*$^{+}$ ISCs), maintains ISC self-renewal, and skews differentiation toward absorptive cell fates, which involves repressing atonal homolog 1 (*Atoh1*) transcription by the hairy and enhancer of split 1 (*Hes1*) transcription factor (Sancho et al., 2015). This sequence of events permits stem cell self-renewal and prevents differentiation to the secretory lineage (Sancho et al., 2015; VanDussen et al., 2012). Indeed, the rapid adoption of early secretory Paneth cell fates by *Hmgcs2*-null ISCs is compatible with a Notch-deficient phenotype (Sancho et al., 2015; Tian et al., 2015), which is confirmed by gene set enrichment analysis (GSEA) in *Hmgcs2*-null versus control ISCs. Notch inhibition-responsive genes were significantly upregulated, and *Atoh1* deletion target genes were significantly downregulated in *Hmgcs2*-null ISCs compared with WT ISCs (Figure 3H; Kim et al., 2014). We validated the induction of *Atoh1* transcripts and the reduction of its negative regulator *Hes1* by ISH in *Hmgcs2*-null intestinal crypt cells compared with controls (Figure 3I). Last, enforced expression of the constitutively active Notch

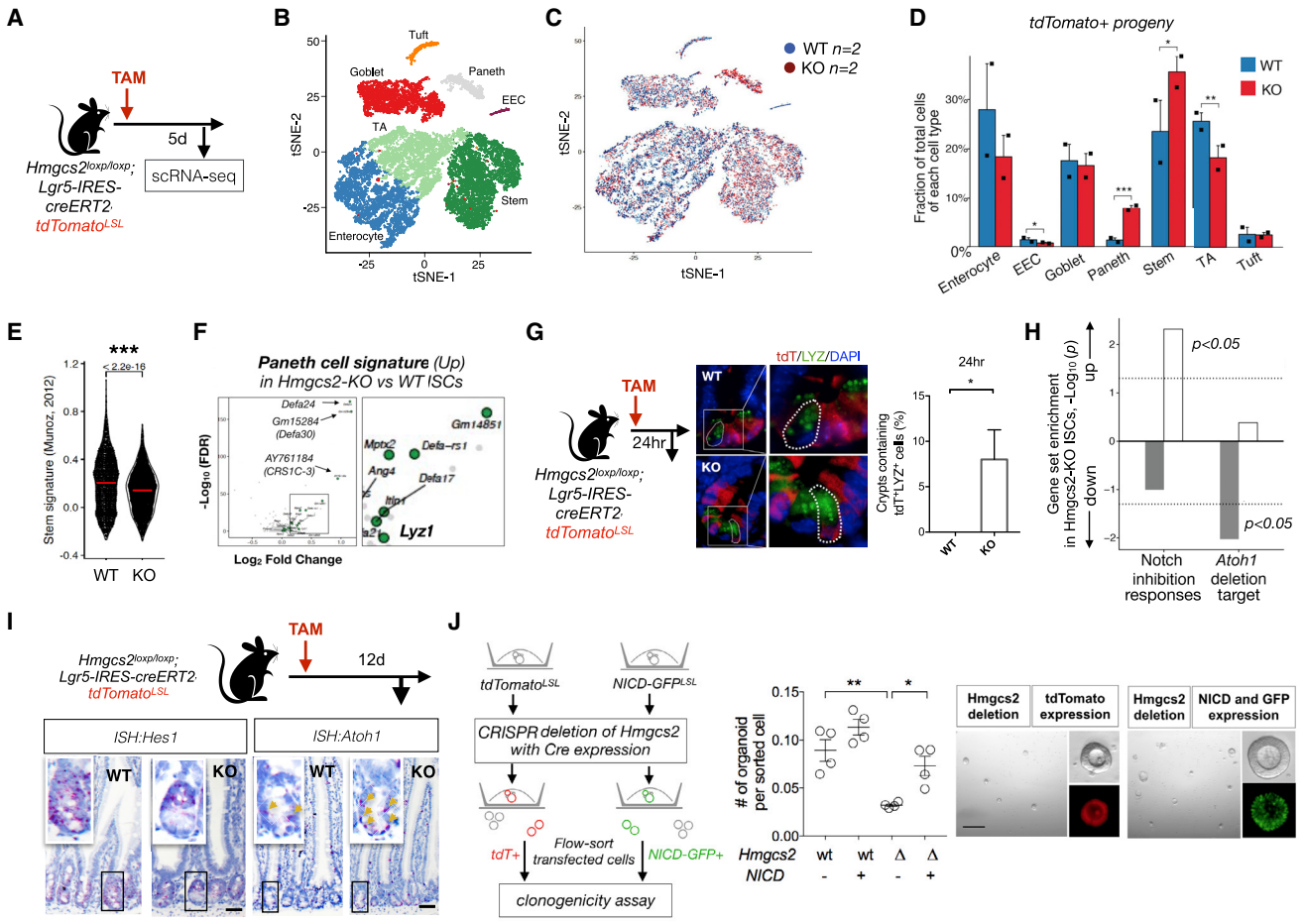


Figure 3. HMGCS2 Regulates Stemness and Secretory Differentiation through Notch Signaling

(A) Schematic of the mouse model, including the timeline of TAM injection and tissue collection for single-cell RNA-seq (scRNA-seq). 5 days after TAM injection, intestinal crypts were isolated from WT and *Hmgcs2*-KO mice, and the *Lgr5*$^{+}$ ISC-derived tdTomato^{+} progeny were flow-sorted for scRNA-seq.

(B) Cell type clusters. We used t-SNE to visualize the clustering (color coding) of 17,162 single cells (*Hmgcs2*-KO, n = 2 mice and 7,793 cells; WT, n = 2 mice and 9,369 cells) based on the expression of known marker genes (Haber et al., 2017). See also Figure S3B. EEC, enteroendocrine cells; TA, transit-amplifying (progenitor) cells.

(C) Merged t-SNE plot of tdTomato^{+} progeny derived from WT (blue) and *Hmgcs2*-KO (red) ISCs.

(D) Fraction of total cells per cell type. Error bars, SEM; * FDR < 0.25, **FDR < 0.1, ***FDR < 0.01; χ^2 test (STAR Methods; Table S2).

(E) Violin plot showing the distribution of the mean expression of the stem cell signature genes (Muñoz et al., 2012) in WT and Hmgcs2-KO ISCs. ***FDR < 0.0001; Mann-Whitney *U* test.

(F) Volcano plot displaying differentially expressed (DE) genes in *Hmgcs2*-KO ISCs versus WT ISCs. 20 of 194 significantly upregulated genes in *Hmgcs2*-KO ISCs are Paneth cell markers (green dots) (Haber et al., 2017). p < 0.0001. n = 2,151 WT ISCs and n = 2,754 KO ISCs.

(G), Representative image and quantification 24 h after TAM injection by immunofluorescence (IF) staining: tdTomato for progeny of *Lgr5*$^{+}$ ISCs and LYZ as a Paneth cell marker. n > 25 crypts per measurement, n > 3 measurements per mouse, and n > 5 mice per group.

(H) Gene Set Enrichment Analysis (GSEA) of Notch inhibition response genes (left) and *Atoh1* deletion target genes (right) (Kim et al., 2014). The barplot of the $-\text{Log}_{10}$ (p value) indicates the gene sets upregulated (white) or downregulated (gray) in *Hmgcs2*-KO ISCs compared with WT ISCs.

(I) Hes family BHLH transcription factor 1 (*Hes1*) and atonal BHLH transcription factor 1(*Atoh1*) mRNA expression in intestinal crypts by ISH. The image represents one of 5 biological replicates per group. Yellow arrows indicate *Atoh1* transcript-positive cells. Scale bar, 50 μm.

(J) Schematic for assessing the organoid-forming ability of genetically engineered organoid cells with CRISPR/Cas9-mediated loss of *Hmgcs2* (left) and constitutive Notch activation by Cre-induced NICD expression (right) or both. Transfected cells were flow-sorted based on the fluorescent markers and plated onto Matrigel (STAR Methods). Organoids were quantified and imaged after 5 days of culture (n = 4 measurements from 2 independent experiments). Scale bar, 200 μm. Data in the dot plot are expressed as mean ± SEM. *p < 0.05 and **p < 0.01.

intracellular domain (NICD) rescued the organoid-forming capacity of *Hmgcs2*-null cells (Figure 3J), supporting the paradigm that HMGCS2 actuates ISCs function through Notch signaling.

βOHB Compensates for *Hmgcs2* Loss in ISCs

HMGCS2 catalyzes the formation of HMG-coenzyme A (CoA) from acetoacetyl-CoA and acetyl-CoA, a rate-limiting step of

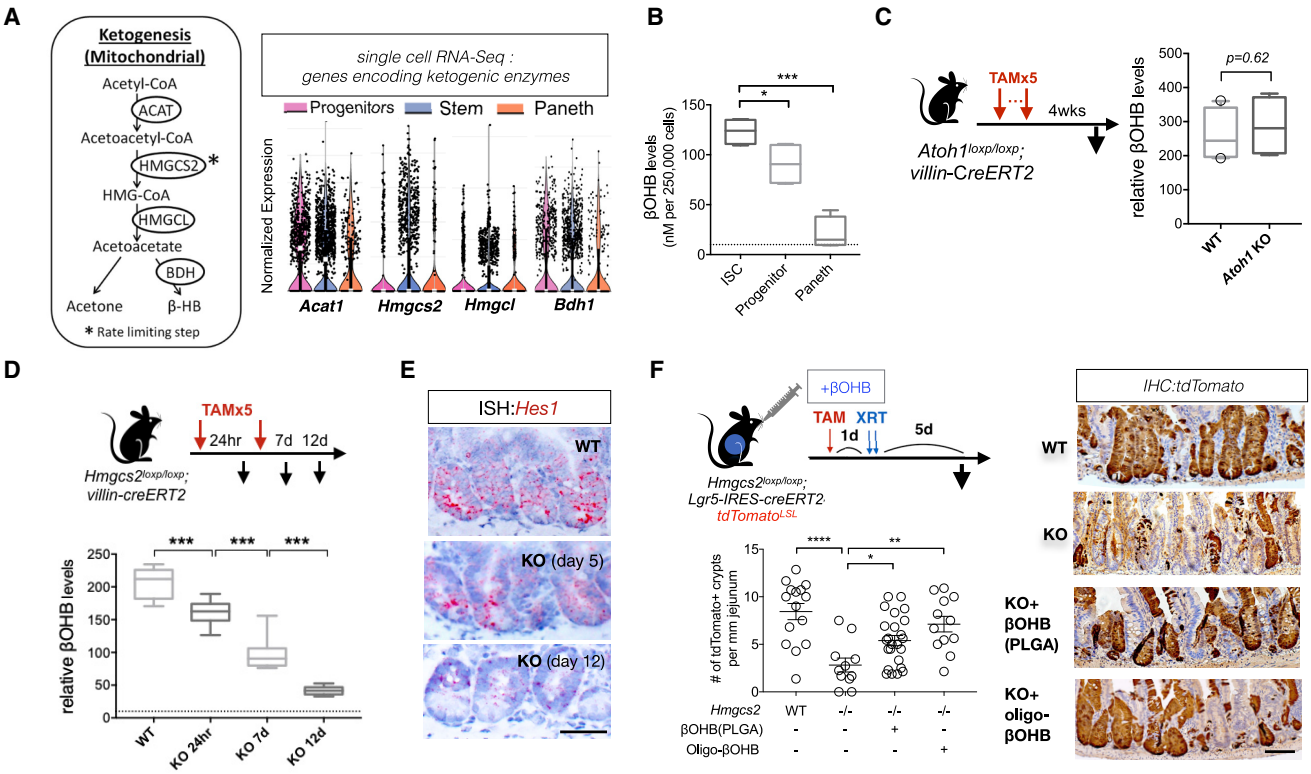


Figure 4. Beta-hydroxybutyrate (βOHB) Compensates for *Hmgcs2* Loss in ISCs

(A) Relative expression of genes encoding enzymes for ketogenesis in ISCs, progenitors, and Paneth cells (Acat 1, acetyl-CoA acetyltransferase 1; Bdh1, 3-hydroxybutyrate dehydrogenase 1; Hmgcl, HMG-CoA lyase), visualized by violin plots for scRNA-seq data. n = 6 mice.

(B) Relative βOHB levels in flow-sorted *Lgr5*-GFP^{hi} ISCs, *Lgr5*-GFP^{low} progenitors, and Paneth cells. 250,000 cells of each cell population were directly sorted into the assay buffer and immediately processed for βOHB measurement. The dashed line indicates the detection limit of the colorimetric assay. n = 8 samples per population from 4 mice.

(C) Schematic for *Atoh1* deletion. 4 weeks after the fifth (last) TAM injection, intestinal tissues were harvested for histology. Intestinal crypts were isolated for βOHB measurement. Shown is quantification of βOHB levels in intestinal crypts from WT and *Atoh1*-KO mice. Levels of βOHB were normalized to total protein of crypt cells. n = 16 samples from 8 mice per group.

(D) Schematic of the mouse model of *Hmgcs2* loss. After TAM injection, intestinal tissues were harvested for histology, and intestinal crypts were isolated for βOHB measurement at the indicated time points (i.e., 24 h, 7 days, and 12 days after the first TAM injection).

(E) *Hes1* mRNA expression in intestinal crypts by ISH at the indicated time points after inducing *Hmgcs2* loss. The image represents one of 5 biological replicates per group.

(F) Schematic (top) of the mouse model, including the timeline of TAM injection, oral administration of nanoparticle PLGA-encapsulated βOHB or βOHB oligomers, irradiation (XRT, 7.5 Gy × 2), and tissue collection. Also shown are quantification (bottom) and representative images (right) of tdTomato^{+} *Lgr5*$^{+}$ ISC-derived lineage (cell progenies) by IHC. Scale bar, 100 μm. n > 25 crypts per measurement, n > 5 measurements per mouse, and n > 3 mice per group.

For box-and-whisker plots (B–D), data were expressed as box-and-whisker 10–90 percentiles. Data in dot plots were expressed as mean ± SEM. *p < 0.05, **p < 0.01, ***p < 0.005, ****p<0.001.

ketone body production (i.e., ketogenesis; Figure 4A). Although *Hmgcs2* was selectively expressed in ISCs compared with progenitors and Paneth cells, genes encoding other ketogenic enzymes, including *acetyl-CoA acetyltransferase 1* (*Acat1*), *Hmg-CoA lyase* (*Hmgcl*), and *3-hydroxybutyrate dehydrogenase 1* (Bdh1) were broadly expressed in both stem and progenitor cells compared with Paneth cells, based on the results of both population (Figure 1A) and scRNA-seq (Figure 4A; Adijanto et al., 2014). Consistent with these expression patterns, measured βOHB levels were highest in *Lgr5*-GFP^{hi} ISCs, followed by *Lgr5*-GFP^{low} progenitors and then Paneth cells (Figure 4B), which was near the detection threshold in sorted intestinal ISCs and progenitors after *Hmgcs2* loss (dotted line in Figure 4B). In addition, genetic ablation of Paneth cells, which provide paracrine metabolites to ISCs (Rodríguez-Colman et al., 2017), in an intestinal *Atoh1*-null model (Durand et al., 2012; Kim et al., 2012) did not alter crypt expression of HMGCS2 protein or βOHB levels (Figures 4C, S4E, and S4F), highlighting that HMGCS2-mediated ketogenesis in crypt cells generates ketone bodies independent of Paneth cells. Finally, genetic ablation of *Hmgcs2* in all intestinal epithelial cells using adult iKO mice diminished βOHB levels over time in crypts (Figure 4D and S4G), with no effect on hepatic HMGCS2 protein expression and serum βOHB levels (Figures S4H and S4I). Interestingly,

crypt βOHB levels after *Hmgcs2* loss also correlated with a decline in *Hes1* ISH expression over time (Figure 4E), highlighting that maximal reduction in Notch activity is observed at the nadir of βOHB depletion.

We recently described a role of fatty acid oxidation (FAO) in the long-term maintenance of *Lgr5*$^{+}$ ISCs, whose end product acetyl-CoA can feed into ketogenesis and other metabolic pathways. Genetic loss of intestinal *Cpt1a* (carnitine palmitoyltransferase I), the rate-limiting step of FAO, resulted in compensatory elevation of HMGCS2 protein expression and in stable crypt βOHB concentrations (Figures S4A–S4D). Conversely, loss of *Hmgcs2* in all intestinal epithelial cells had no effect on intestinal CPT1a protein levels or on FAO in *Hmgcs2*-null crypts (Figures S4J and S4K). Although intestinal loss of either *Cpt1a* or *Hmgcs2* diminishes *Lgr5*$^{+}$ ISC numbers, *Cpt1a* loss has no effect on intestinal differentiation (Mihaylova et al., 2018), whereas *Hmgcs2* loss skews differentiation toward the secretory lineage (Figures 2E, 2F, 3G, S2G and S3H). Taken together, these findings indicate that FAO and ketogenesis maintain intestinal stem and progenitor cell activity partly through independent mechanisms.

We next examined whether βOHB rescues the function and secretory differentiation phenotype of *Hmgcs2*-null organoids. To address this question, we administered tamoxifen to control and *Hmgcs2*$^{loxp/loxp}$*; Lgr5*-tdTomato lineage tracer mice 24 h before crypt isolation (Figure S4L). Crypts with *Hmgcs2*-null ISCs were then cultured in standard medium with or without βOHB. Compared with controls, crypts with *Hmgcs2*-null ISCs were 34.4% less capable of forming organoids, and the resulting organoids showed a 40.5% increase in goblet cells and a 64.3% decline in tdTomato^{+} cells per organoid (Figure S4L). These results indicate that *Hmgcs2*-null ISCs *in vitro* are less functional and biased toward secretory differentiation, as seen *in vivo*. Exogenous βOHB, but not lactate, a Paneth niche-derived metabolite that sustains ISC function (Rodríguez-Colman et al., 2017), rectified these functional deficiencies (i.e., organoid-forming capacity and generation of tdTomato^{+} clones) and the secretory lineage bias of *Hmgcs2*-null organoids (Figures S4L and S4M). To investigate whether βOHB also compensates for the loss of intestinal HMGCS2 activity *in vivo*, we developed and delivered two modified forms of βOHB to the gastrointestinal tract of *Hmgcs2* intestinal knockout (Lgr5 lineage tracer KO model) mice (Figure S4N). Oral administration of poly(lactic-co-glycolic acid) (PLGA) encapsulated βOHB nanoparticles or βOHB oligomers (Figure S4N) partially restored intestinal regeneration after irradiation-induced damage, which otherwise was severely impaired upon *Hmgcs2* intestinal deletion (Figure 4F). Thus, βOHB is sufficient to substitute for HMGCS2 activity in ISCs and may serve as a biochemical link between the HMGCS2 and Notch signaling pathways.

βOHB-Mediated Class 1 Histone Deacetylase (HDAC) Inhibition Enhances Notch Signaling

HMGCS2 is a mitochondrial matrix enzyme and unlikely to physically interact with the Notch transcriptional machinery, so we explored the regulatory role of its metabolic product βOHB, which has been reported to be an endogenous inhibitor of class I HDACs (Shimazu et al., 2013). Although the link between HDAC and Notch signaling is not well delineated in the mammalian intestine, experimental evidence in model organisms (Yamaguchi et al., 2005) and in other tissues (Hsieh et al., 1999; Kao et al., 1998; Oswald et al., 2002) suggests that HDACs can transcriptionally repress Notch target genes. Consistent with this possibility, an earlier study found that addition of HDAC inhibitors to organoid cultures decreases the niche dependency of *Lgr5*$^{+}$ ISCs partly through Notch activation (Yin et al., 2014). Our published population-based RNA-seq and scRNA-seq dataset (Haber et al., 2017; Data and Code Availability) revealed that Notch receptor (e.g., *Notch1*), Hdac (e.g., *Hdac1*, *Hdac2*, and *Hdac3*), and Notch target genes (e.g., *Hes1*) are enriched in ISCs and that REACTOME_ NOTCH1_ INTRACELLULAR_ DOMAIN_ REGULATES_ TRANSCRIPTION, which includes Notch and Hdacs, ranked as the second-highest signature of ISCs from the MSigDB c2 collection of 2,864 transcriptional pathways (Figures 5A and S5A). These analyses indicate that ISCs display high Notch activity despite high expression of repressive Hdacs. To test whether enzymatic inhibition of HDACs by βOHB activates Notch target gene expression such as *Hes1*, we exposed *Hes1*-GFP organoids to the βOHB and HDAC1 inhibitor quisinostat (JNJ-26481585 [JNJ]) (Figure 5B). Both interventions increased GFP expression compared with the control, whereas, as expected, treatment with a γ-secretase inhibitor (GSI; a NOTCH inhibitor) dampened GFP expression.

Next we treated *Hmgcs2*-null organoids with βOHB, HDAC inhibitors, or both and assessed the role of Notch in this process by treating a subset of cultures with GSI. Strikingly, we found that the HDAC inhibitor quisinostat (JNJ) at a dose shown to block HDAC1 activity (Arts et al., 2009), as did CRISPR deletion of Hdac1 (Figures 5C and S5G), rescued crypt organoid-forming capacity better than the more promiscuous pan-HDAC class I and II inhibitor trichostatin A (TSA) (Figures 5C and S5F). Also, co-treatment with JNJ and βOHB did not further augment crypt organoid-forming capacity, demonstrating redundancy between βOHB signaling and HDAC inhibition (Figure 5C, left). Blockade of Notch signaling by GSI treatment prevented the ability of either βOHB or the JNJ HDAC inhibitor (Figure 5C, right) to restore the organoid-forming capacity of *Hmgcs2*-null crypts, indicating that βOHB and HDAC inhibition regulate ISC function through NICD-mediated transcriptional activity (Figure 7F). In parallel experiments, treatment with an HDAC1/3 inhibitor (MS-275, 10–100 nM) rescued *Hmgcs2*-null organoid function; however, doses beyond this range (Zimberlin et al., 2015) failed to do so (Figure S5F).

To bolster the connection between HMGCS2-mediated control of HDAC activity and Notch signaling *in vivo*, we found that *Hmgcs2* loss and ketone depletion (Figure 4D) decreased the numbers of H3K27ac- or NICD-positive crypt cell nuclei, which correlates with greater HDAC activity and less Notch signaling (Figures 5D and S5H). Consistent with the paradigm that βOHB hinders HDAC1 activity, robust *in vivo* induction of

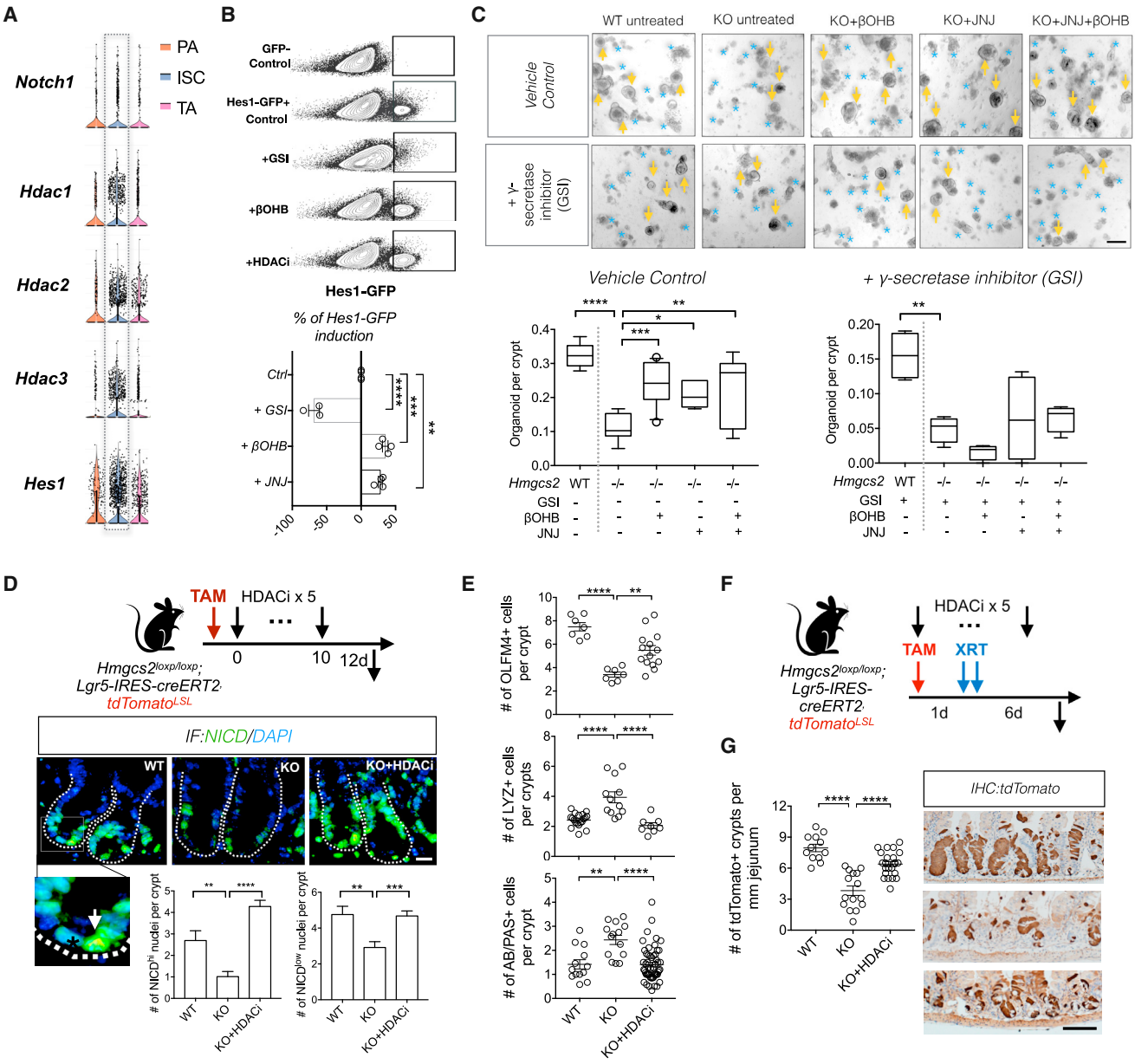


Figure 5. βOHB-Mediated HDAC Inhibition Enhances Notch Signaling

(A) Violin plots of genes related to Figure S5A: Notch receptor Notch1, class I HDAC genes (*HDAC1/2/3*), and the Notch target *Hes1* based on a previously published scRNA-seq data (Haber et al., 2017).

(B) Representative flow cytometry plots (top) and quantification of GFP-expressing (bottom) *Hes1*-GFP$^+$ primary organoids exposed to the γ-secretase inhibitor (GSI; 10 μM), βOHB (50 μM), and an HDAC inhibitor (JNJ-26481585, 0.2 nM) compared with the control condition. n = 6 samples per treatment from n = 3 mice.

(C) Organoid-forming assay for intestinal crypts isolated from WT and *Hmgcs2*-KO mice, with combinations of the HDAC inhibitor JNJ-26481585 (JNJ) or βOHB treatments or the Notch receptor cleavage inhibitor (GSI). Quantification and representative images show day 5–7 organoids. n = 4 mice. Scale bar, 500 μm. Arrows indicate organoids, and asterisks indicate aborted crypts.

(D) Schematic (top) of the mouse model, including the timeline of TAM and HDAC inhibitor (HDACi; JNJ) injection and tissue collection. Quantification of nuclear NICD (cleaved NOTCH1 receptor) by IF. Inset: the arrow indicates the NICD^{high} nucleus, and the asterisk indicates the NICD^{low} nucleus. Data (bottom) represent n > 25 crypts per measurement, n > 3 measurements per mouse, and n > 3 mice per group. Scale bar, 20 μm.

(E) Quantification of OLFM4$^+$ stem cells, LYZ$^+$ Paneth cells, and AB/PAS$^+$ goblet cells in proximal jejunal crypts by IHC.

(F) Schematic of the mouse model, including a timeline of TAM and HDACi (JNJ) injection, irradiation (XRT, 7.5 Gy × 2), and tissue collection.

(G) Quantification and representative images of tdTomato$^+$ *Lgr5*$^+$ ISC-derived lineage (cell progenies) by IHC. Scale bar, 100 μm. n > 25 crypts per measurement, n > 3 measurements per mouse, and n > 5 mice per group.

For box-and-whisker plots (C), data were expressed as box-and-whisker 10–90 percentiles. Data in the bar graph (D) and dot plot (E and G) are expressed as mean ± SEM. *p < 0.05, **p < 0.01, ***p < 0.005, ****p < 0.0001.

Hmgcs2 (Mihaylova et al., 2018; Tinkum et al., 2015) and βOHB levels in the crypts with a 24-h fast (Figure S5B) were associated with greater H3K27ac enrichment peaks compared with controls by chromatin immunoprecipitation sequencing (ChIP-seq) (Figure S5C). Moreover, this trend also holds true at gene enhancer and promoter sites (±5 kb TSS), including at *Hes1* (Figures S5D and S5E). Importantly, HDAC inhibitor treatment (JNJ, 1 mg/kg, 5 intraperitoneal [i.p.] injections) of *Hmgcs2*-null mice not only prevented these changes (Figures 5D and S5H) but also rescued the decline in ISC numbers (Figure 5E), ISC function after injury (Figures 5F and 5G), and the expansion of secretory cell types (Figure 5E; Figure S5I). These data collectively support the notion that βOHB drives the downstream effects of HMGCS2 through inhibition of class I HDACs to stimulate Notch signaling for stemness (Figure 7F).

A Ketogenic Diet Boosts ISC Numbers and Function

Because HMGCS2-derived ketones in ISCs promote self-renewal and prevent premature differentiation, we asked whether a ketogenic diet (KTD; STAR Methods), an intervention that dramatically elevates circulating ketone body levels (Newman et al., 2017), enhances ISC numbers, function, or both. *Lgr5*$^{+}$ reporter mice fed a KTD for 4–6 weeks show no change in body mass, intestinal length, or crypt depth and have a 3.5-fold increase in serum βOHB level compared with chow controls (Figures 6A and S6A–S6D). In the intestine, a KTD pronouncedly not only boosted HMGCS2 protein expression throughout the entire crypt/villous unit (Figures 6A), which correlated with a 6.8-fold elevation in crypt βOHB concentrations (Figure 6B), but also enhanced Notch activity by 2-fold, as measured by flow cytometry for HES1-GFP positivity (Figure 6C), NICD nuclear localization (Figure S6F), and OLFM4 protein expression (a Notch target gene; Figure S6E) (Tian et al., 2015; VanDussen et al., 2012). In addition, KTD mice had greater numbers of *Lgr5*-GFP^{hi}/OLFM4^{+} ISCs and *Lgr5*-GFP^{low} progenitors (Figures 6D and S6E) with slightly higher rates of proliferation for ISCs but not for progenitor cells, as determined after a 4-h bromodeoxyuridine (BrdU) pulse (Figure S6H).

Not only did a KTD lead to quantitative changes in ISCs, both KTD crypts and KTD-derived ISCs in Paneth cell co-culture assays were more capable of forming organoids compared with controls (Figures 6E and S6G). Similarly, a KTD also boosted the regenerative output of tdTomato-labeled ISCs after radiation-induced damage relative to their chow counterparts (Figure 6F). Because exogenous ketones rectify *Hmgcs2* loss *in vitro* (Figure S4L) and *in vivo* (Figure 4F), liver or other non-intestinal sources of ketones may substitute for or supplement ISC-generated ketones in KTD-mediated regeneration (Figure 4F), where circulating ketone levels are highly elevated (Figure S6B). To distinguish between the contribution of circulating ketones versus intestinal ketones in this process, we engineered *Hmgcs2*$^{loxp/loxp}$*; UBC-CreERT2* conditional whole-body KO mice that disrupts *Hmgcs2* in all adult cell types upon tamoxifen administration (Figure 6G; termed wKO). Although *Hmgcs2* loss in the iKO model significantly lowered crypt βOHB levels in a KTD, it was still higher than levels noted in control iKO crypts (Figure 6G). This difference is likely due to uptake of circulating ketones induced by the KTD (Figure 6G) because crypt βOHB levels were undetectable in control or KTD crypts from wkO mice (Figure 6G). Remarkably, this pattern of crypt βOHB concentration mirrored the numbers of intact surviving crypts after radiation-induced intestinal epithelial injury (Figure 6H). Although the pro-regenerative effects of a KTD were blunted by intestinal *Hmgcs2* loss, they were entirely blocked with whole-body *Hmgcs2* loss, demonstrating that βOHB regulates ISCs in a cell-autonomous and non-autonomous manner in ketogenic states (Figure 6H).

Although exogenous βOHB in a KTD restored the *in vivo* lineage differentiation defects and crypt organoid-forming capacity in *Hmgcs2*-null intestines (Figure S6M), neither a KTD nor exogenous βOHB exposure in wild-type intestines or organoids affected secretory cell lineage differentiation (Figures S6I–S6L). This finding indicates that, although surplus intestinal βOHB bolsters ISC self-renewal (i.e., ISC numbers, proliferation, and *in vitro* and *in vivo* function) and Notch signaling, it is not sufficient to suppress secretory differentiation in *Hmgcs2*-compentent ISCs. This disconnect between excessive (i.e., supraphysiologic) Notch activity in driving stemness but not in inhibiting secretory differentiation has been documented previously in conditional genetic models of enforced Notch signaling in the adult intestine (Vooijs et al., 2011; Zecchini et al., 2005).

A Glucose-Supplemented Diet Dampens Intestinal Ketogenesis and Stemness

Ketogenesis is an adaptive response to dietary shortages of carbohydrates where, in low carbohydrate states, liver-derived ketone bodies are utilized by peripheral tissues for energy (Newman and Verdin, 2017; Puchalska and Crawford, 2017). In the presence of dietary glucose, for example, hepatic HMGCS2 expression and ketone body production rapidly switch off in response to insulin (Cotter et al., 2013). To investigate how a glucose-supplemented diet alters ISCs, we fed mice a chow diet with glucose-supplemented drinking water (13% glucose in drinking water *ad libitum*) for 4 weeks (Figure 7A), where mice consumed 2.68 ± 0.5 mL of the glucose solution (per mouse per day). Although 4-week glucose supplementation did not induce obesity (Figure S7A), this regimen significantly diminished HMGCS2 expression at the crypt base (Figure 7A) and reduced crypt βOHB levels (Figure 7B). This dietary suppression of intestinal ketogenesis was accompanied by a 2-fold decrease in *Hes1* expression, confirming that Notch activity correlates with βOHB concentrations (Figure 7C). Similar to intestinal *Hmgcs2* loss (Figure 2), mice on this regimen had 3-fold fewer OLFM4^{+} ISCs and greater Lyz1^{+} Paneth cell and AB^{+} goblet cell numbers (Figures S7B–S7D). Functionally, a 2-week course of glucose supplementation hampered the ability of ISCs to generate tdTomato^{+}-labeled progeny by 2-fold in a lineage tracing experiment with radiation-induced injury (Figure 7D) and separately decreased surviving intact crypt numbers compared with controls (Figure 7E). These functional deficits could be rescued by a single oral bolus of βOHB

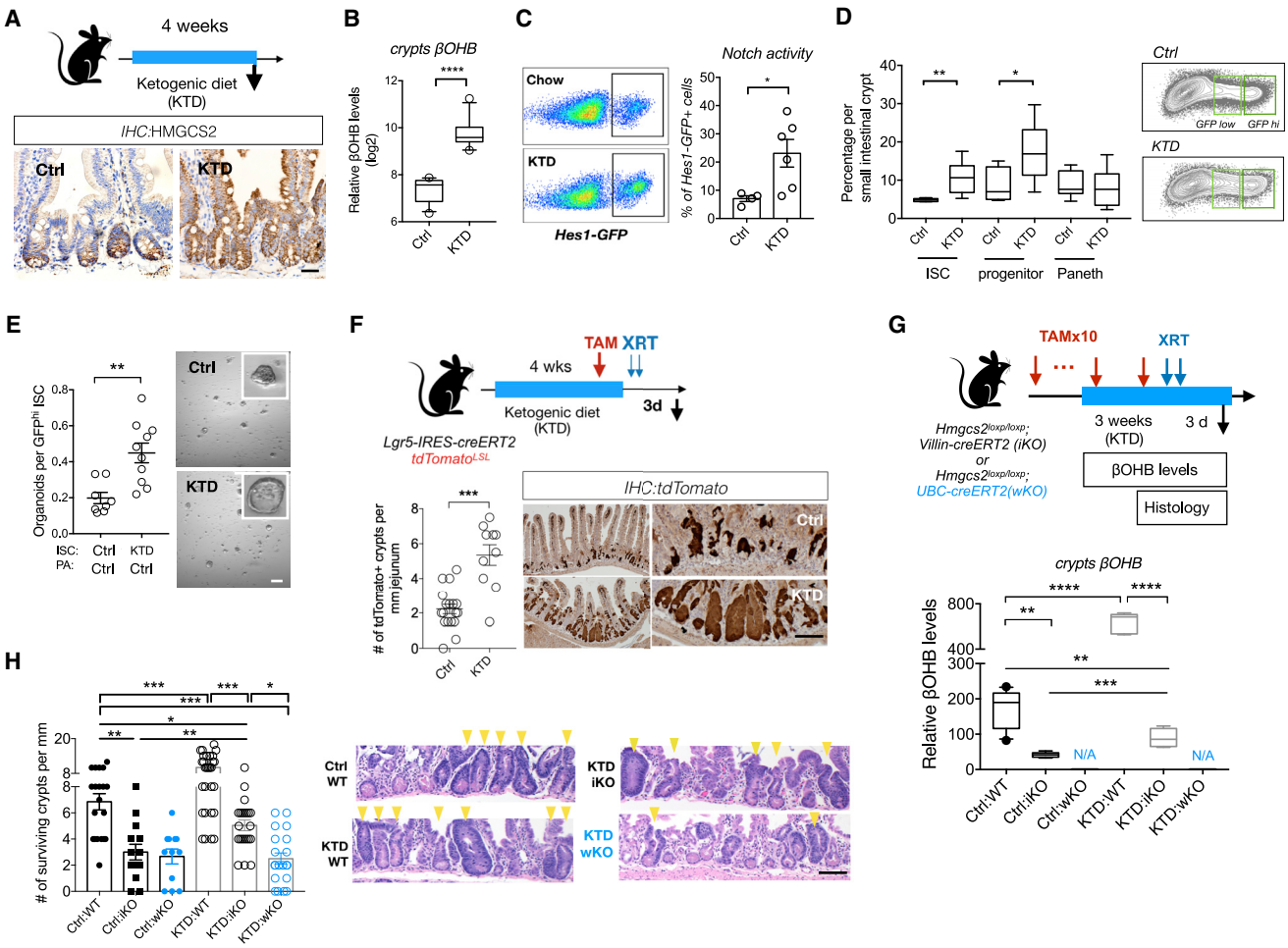


Figure 6. A Ketogenic Diet Enhances ISC Self-Renewal in an HMGCS2-Dependent manner

(A) Schematic (top) of the mouse model, including the timeline of the ketogenic diet (KTD) and tissue collection. After 3–4 weeks of the diet, intestinal tissues of KTD-fed or chow-fed (Ctrl) mice were harvested for histology or crypt culture or sorted by flow cytometry for cell frequency analysis. n > 5 mice per group. Bottom: HMGCS2 expression by IHC. The image represents one of 5 biological replicates. Scale bars, 50 μm.

(B) βOHB levels in intestinal crypts from KTD- and chow-fed mice. Levels of βOHB were normalized to total protein of crypt cells. n = 12 samples from 6 mice per group.

(C) *Hes1*-GFP expression, a measure of Notch activation by flow cytometry, of crypt cells from KTD- and chow-fed mice.

(D) Frequencies of *Lgr5*-GFP^{hi} ISCs, *Lgr5*-GFP^{low} progenitors, and CD24^{+}c-Kit^{+} Paneth cells in crypts from KTD- and chow-fed mice. n = 6 mice per group.

(E) Organoid-forming assay for sorted ISCs from KTD- and chow-fed mice co-cultured with Paneth cells from chow-fed mice. n = 6 mice per group. Representative images show day 5 organoids. Scale bar, 100 μm.

(F) Schematic (top) of the Lgr5 lineage tracing, including a timeline of TAM injection, irradiation (XRT, 7.5 Gy × 2), and tissue collection. Intestinal tissues were harvested for histology, and intestinal crypts were isolated for βOHB measurement at the indicated time points. Shown are quantification and representative images (bottom) of tdTomato^{+} *Lgr5*$^{+}$ ISC-derived progeny labeled by IHC for tdTomato.

(G and H) Schematic (G, top) of intestinal *Hmgcs2* deletion (iKO) and whole-body *Hmgcs2*-deletion (wKO) mice on the KTD, including a timeline of TAM injection, irradiation (XRT, 7.5 Gy × 2), and tissue collection (G). Also shown are βOHB levels (G, bottom) in intestinal crypts isolated from the indicated groups and number of surviving crypts assessed by the microcolony assay (H).

In (F) and (H), scale bars, 100 μm; n > 25 crypts per measurement, n > 5 measurements per mouse, and n > 3 mice per group. Data in dot plots (C, E, and F) are expressed as mean ± SEM. In (B), (D), and (G), shown are box-and-whisker 10–90 percentiles. *p < 0.05, **p < 0.01, ****p < 0.001.

(15 mg/25 g βOHB oligomers 16 h prior to irradiation) (Figures 7D and 7E). These results illustrate that dietary suppression of βOHB production mimics many aspects of *Hmgcs2* loss and that exogenous ketone bodies can compensate for these deficits.

DISCUSSION

Our data favor a model in which small intestinal *Lgr5*$^{+}$ ISCs express the enzyme HMGCS2, which produces ketone bodies, including acetoacetate, acetate, and βOHB, to

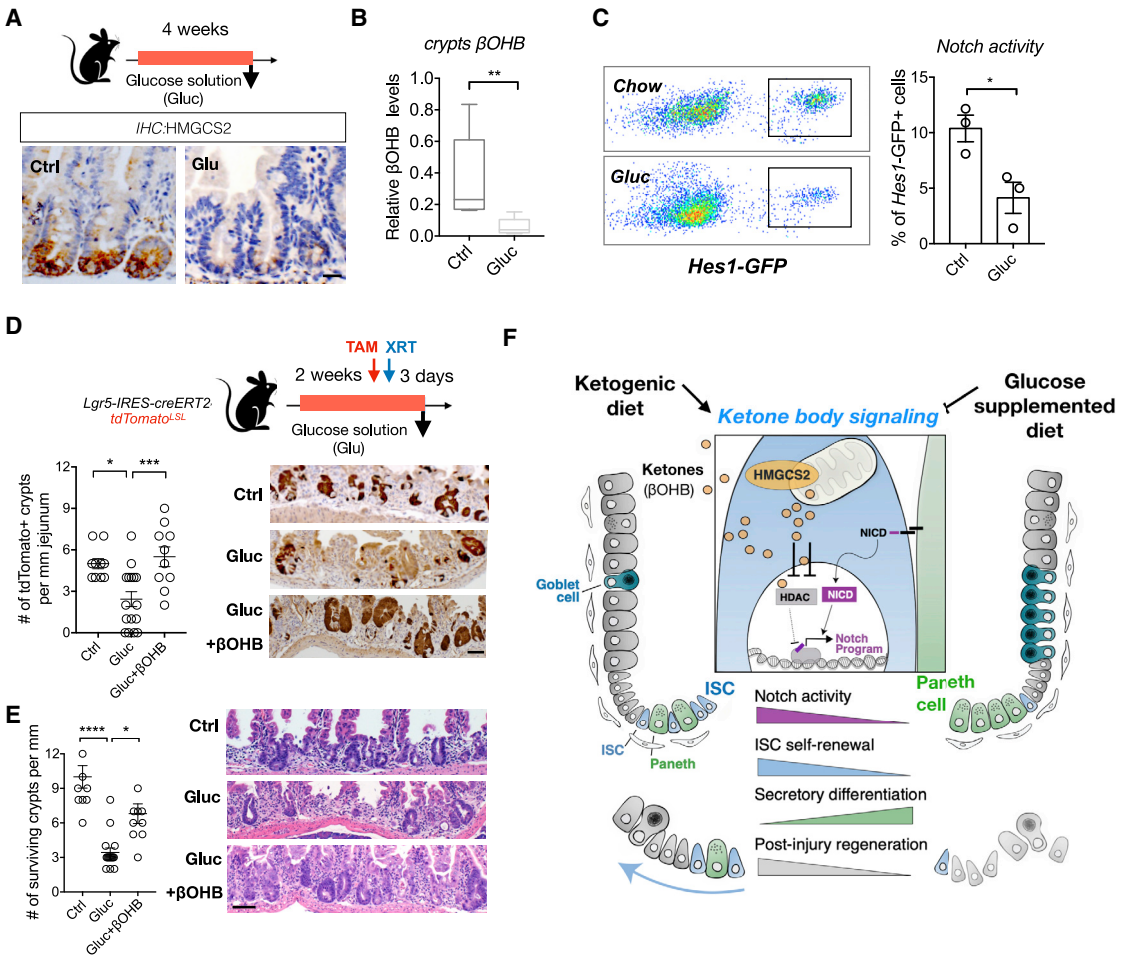


Figure 7. Dietary Glucose Dampens Intestinal Ketogenesis and Stemness

(A) Schematic (top) of the mouse model, including the timeline of glucose (Gluc) supplementation and tissue collection. After 3–4 weeks of the diet, intestinal tissues of Gluc and Ctrl mice were harvested for histology or crypt culture or sorted by flow cytometry for cell frequency analysis. n > 5 mice per group. Bottom: HMGCS2 expression by IHC. The image represents one of 5 biological replicates. Scale bars, 50 μm.

(B) βOHB levels in intestinal crypts from Gluc and Ctrl mice. Levels of βOHB were normalized to total protein of crypt cells. n = 12 samples from 6 mice per group.

(C) *Hes1*-GFP expression, a measure of Notch activation by flow cytometry, of crypt cells from Gluc and Ctrl mice.

(D and E) Schematic (D, top) of the *Lgr5* lineage tracing, including a timeline of TAM injection, irradiation (XRT, 7.5 Gy × 2), and tissue collection. Also shown is quantification and representative images (D, bottom) of tdTomato$^+$ *Lgr5*$^+$ ISC-derived progeny labeled by IHC for tdTomato and the number of surviving crypts assessed by the microcolony assay (E). Scale bars, 100 μm. n > 25 crypts per measurement, n > 5 measurements per mouse, and n > 3 mice per group.

(F) Model of how ketone body (βOHB) signaling dynamically regulates intestinal stemness in homeostasis and in response to diet. In normal dietary states, mitochondrial HMGCS2-derived βOHB enforces Notch signaling through HDAC class 1 inhibition. Genetic ablation of *Hmgcs2* reduces ISC βOHB levels, thereby increasing HDAC-mediated suppression of the Notch transcriptional program, which diminishes ISC numbers and function and skews differentiation toward the secretory lineage. Ketogenic diets (KTDs) enhance both systemic and stem cell-produced βOHB levels in ISCs, leading to higher Notch activity, ISC function, and post-injury regeneration. In contrast, glucose-supplemented diets suppress ketogenesis and have the opposite effects on intestinal stemness. Thus, we propose that dynamic control of ISC βOHB levels enables it to serve as a metabolic messenger to execute intestinal remodeling in response to diverse physiological states.

regulate intestinal stemness (Newman and Verdin, 2017; Figure 6H). Although ketone bodies are known to provide energy to tissues during periods of low-energy states, such as fasting or prolonged exercise, they have also been implicated as signaling metabolites that inhibit the activity of class I HDACs (Newman and Verdin, 2017; Shimazu et al., 2013). A recent study (Wang et al., 2017) implicated HMGCS2-mediated ketogenesis in promoting secretory differentiation with loss-of-function studies in immortal colon cell lines and a ketone body supplemented diet, which contrasts with our findings. This discrepancy may represent regional differences between the small intestine and colon and also highlights the importance of robust *in vivo* loss-of-function models, where we generated separate alleles that target *in vivo Hmgcs2*

expression (i.e., the lacZ and loxp models) (Wang et al., 2017). Here we identify novel roles of βOHB as a signaling metabolite in *Lgr5*$^+$ ISCs that facilitates Notch signaling—a developmental pathway that regulates stemness and differentiation in the intestine—through HDAC inhibition (Figure 7F). Thus, we propose that dynamic control of βOHB levels in ISCs enables this metabolic messenger to execute rapid intestinal remodeling in response to diverse physiological states (Figure 7F).

A challenge is how to optimally model and reconcile βOHB-mediated partial class 1 HDAC enzymatic inhibition with genetic loss-of-function approaches in the intestine. Two independent groups (Gonneaud et al., 2015; Zimberlin et al., 2015) demonstrated loss of secretory differentiation with combined *Hdac1* and *Hdac2* intestinal loss, which is consistent with a Notch phenotype and our model (Figure 6H). However, these two groups came to different conclusions regarding how loss of *Hdac1* and *2* affect crypt proliferation, with one model (Gonneaud et al., 2015) showing crypt hyperplasia and proliferation using an inducible intestine-specific *Villin-CreERT2* allele and the other model (Zimberlin et al., 2015) showing crypt loss and reduced proliferation using an inducible Ah-Cre allele that is expressed in the intestine and liver. The Ah-Cre model reportedly (Gonneaud et al., 2015) causes greater DNA damage and is not specific to the intestine, which cannot exclude non-intestinal effects. Regardless, as proposed by others (Haberland et al., 2009), genetic ablation of *Hdac* members irreversibly eliminates HDAC enzymatic activity and permanently disrupts all complexes seeded by HDACs throughout the genome. In contrast, HDAC inhibitors, similar to βOHB, temporarily inhibit enzymatic activity without abolishing the co-repressor complexes (Haberland et al., 2009); thus, pharmacologic or βOHB-mediated reversible inhibition of HDACs need not phenocopy permanent genetic loss *in vivo*.

Many lines of evidence indicate that Notch signaling is undergirding the effects of HMGCS2 in *Lgr5*$^+$ ISCs. First, *Hmgcs2* loss leads to a gradual decrease in the expression and number of OLFM4$^+$ cells within the crypt (Figure 2D), which is a stem cell marker dependent on Notch signaling (VanDussen et al., 2012). Second, *Hmgcs2* loss emulates many of the characteristics of intestine-specific *Notch1* deletion, with expansion in goblet and Paneth cell populations (Figures 2E, 2F, S2G, and 3A–3H; Fre et al., 2005; Kim et al., 2014; Sancho et al., 2015; Yang et al., 2001). Third, *Hmgcs2* loss dampens Notch target gene expression, perturbs Notch-mediated lateral inhibition (Figures 3H and 3I), and primes ISCs to adopt an early Paneth cell fate (Figures 3F, 3G, S3G, and S3H). Last, these deficits correlate with a reduction in the number of NICD-positive intestinal crypt cell nuclei (Figure 5D), and constitutive Notch activity remedies *Hmgcs2*-null organoid function (Figure 3J).

Because *Lgr5*$^+$ ISCs receive Notch ligand stimulation (e.g., Dll1 and Dll4) from their Paneth cell niche, an important question is why small intestinal *Lgr5*$^+$ ISCs reinforce Notch signaling with endogenous ketones. One possible answer is that stem cells, in contrast to lateral Notch inhibition in non-ISC progenitor cells that are higher up in the crypt, depend on greater Notch activity to maintain stemness and prevent their premature differentiation into Paneth cells (Figures 3G and S3G). These redundant pathways that stimulate Notch signaling in *Lgr5*$^+$ ISCs may, for example, permit these cells to persist when Paneth cells are depleted with diphtheria toxin (Sato et al., 2011) or in other genetic models (Durand et al., 2012; Kim et al., 2012; Yang et al., 2001), such as with intestinal *Atoh1* loss (Figures 4C, S4E, and S4F).

Another possibility is that systemic and intestinal βOHB production provides a signaling circuit that couples organismal diet and metabolism to intestinal adaptation (Barish et al., 2006; Beyaz et al., 2016; Ito et al., 2012; Narkar et al., 2008). For example, we reported previously that diets that induce ketogenic states, such as fasting (Mihaylova et al., 2018), high-fat diets (Beyaz et al., 2016), and ketogenic diets (Figures 6 and 7E) strongly induce PPAR transcriptional targets in ISCs, which also includes *Hmgcs2* (Figure S2E). Furthermore, these ketogenic states coordinately drive βOHB production in the liver (which accounts for circulating levels) and in the intestine, which both then stimulate a ketone body-mediated signaling cascade in stem cells that bolsters intestinal regeneration after injury (Figures 6F–6H and 7F). In ketogenic states, we propose that PPAR activated ketogenesis reinforces Notch signaling through BOHB mediated HDAC inhibition (Figure 7F). Supporting this supposition, we find that a ketogenic diet boosts not only crypt βOHB levels but also ISC numbers and function and Notch signaling. The converse occurs in glucose-rich diets, where βOHB levels are suppressed, as are ISC numbers and function and Notch signaling. An interesting aspect of our work is to understand the cancer implications of ISC-promoting ketogenic diets, given that some intestinal cancers arise from ISCs (Barker et al., 2009) and that ketogenic diets in some mouse strains improve health and mid-life survival (Newman et al., 2017). Future studies will need to further explore (1) the cancer consequences of our model, (2) the energetic and Notch-independent signaling roles ketone bodies play in intestinal stemness and, (3) the non-cell-autonomous roles of ISC-derived ketone bodies on stromal, immune, and microbial elements in the stem cell microenvironment.

STAR★METHODS

Detailed methods are provided in the online version of this paper and include the following:

- KEY RESOURCES TABLE
- LEAD CONTACT AND MATERIALS AVAILABILITY
- EXPERIMENTAL MODEL AND SUBJECT DETAILS
  - Animal
  - Organoids
  - Human intestinal samples
- METHOD DETAILS
  - *In vivo* treatments
  - Beta-Hydroxybutyrate (βOHB) measurements
  - Crypt Isolation and culturing
  - RT-PCR and *In Situ* Hybridization (ISH)

- Immunostaining and Immunoblotting
- 13C-Palmitate labeling and LC/MS Methods
- Population RNA-Seq analysis
- GSEA analysis of bulk RNA-Seq
- Droplet scRNA-seq
- Droplet scRNA-seq data processing
- ChIP-sequencing analysis

- QUANTIFICATION AND STATISTICAL ANALYSIS
- DATA AND CODE AVAILABILITY

SUPPLEMENTAL INFORMATION

Supplemental Information can be found online at https://doi.org/10.1016/j.cell.2019.07.048.

ACKNOWLEDGMENTS

We thank Fang Wang for providing βOHB oligomers. We thank Dr. Julien Sage and Dr. Spyros Artavanis-Tsakonas for the generous gift of Hes1-GFP reporter mice. We thank Sven Holder for histology support, the Whitehead Institute Metabolite profiling core facility, and the Koch Institute Flow Cytometry, Histology, and ES Cell and Transgenics core facilities. We thank Leah Bury for illustration assistance, members of the Yilmaz laboratory for discussions, and Kerry Kelley for laboratory management. Ö.H.Y. is supported by NIH R00 AG045144, R01CA211184, R01CA034992, and U54CA224068; a V Foundation V scholar award; a Sidney Kimmel scholar award; a Pew-Stewart Trust scholar award; the Kathy and Curt Marble Cancer Research Fund; a Bridge grant; the American Federation of Aging Research (AFAR); and the MIT Stem Cell Initiative through Fondation MIT. C.W.C. is supported by a Ludwig postdoctoral fellowship and a Helen Hay Whitney postdoctoral fellowship. N.G is supported by a TUBITAK-BIDEB 2214-A fellowship. G.C.-K. is supported by a TUBITAK 2219 international postdoctoral research fellowship. We thank the members of The Hope Babette Tang (1983) Histology Facility at the Koch Institute. S.R. was supported by a postdoctoral fellowship from the MIT Ludwig Center for Molecular Oncology Research, NIH grant U54-CA163109, and the Howard Hughes Medical Institute (to R.O.H.). A.R. is supported by the Klarman Cell Observatory and HHMI. M.M.M. is supported by NIH R00 AG054760. A.R. is a SAB member of Thermo Fisher Scientific, Driver Group, and Syros Pharmaceuticals and a co-founder of Celsius Therapeutics. We would like to thank Kerry Kelly for excellent lab management.

AUTHOR CONTRIBUTION

C.-W.C. conceived, designed, performed, interpreted all of the experiments and wrote the manuscript with Ö.H.Y. M.B. performed single-cell RNA-seq, and A.L.H. conducted statistical analysis with support from A.R. C.T. performed ChIP sequencing and data analysis with support from H.P.-W. and K.R. N.G., S.T., M.M., A.M.I., K.E.B.-R., S.I., and M.S.U. performed *Hmgcs2* deletion and dietary experiments. G.E. designed and prepared modified βOHB for *in vivo* experiments. L.T.G. performed *Atoh1* intestinal deletion experiments and participated in experimental design and data analysis. C.M. and L.A.B. assisted with the data analysis. G.C.-K. and S.R. performed histopathological examination and provided diagnostic information with support from Y.B., M.M.-K., V.D., and R.O.H. M.M.M. contributed to gene expression profiling and to the development of crypt metabolomic assays for FAO analysis. M.T.W. provided animal research facility support and assisted in the design and interpretation of experiments with support from J.G.F. V.L.B. performed bioinformatics analysis with support from S.S.L. All of the authors assisted in the interpretation of the experiments and the writing of the paper.

DECLARATION OF INTERESTS

Ö.H.Y is a consultant of Merck. The authors have a provisional patent application (US Provisional filing serial Nno. 62/855915, filed May 31, 2019).

Received: January 7, 2019
Revised: June 3, 2019
Accepted: July 25, 2019
Published: August 22, 2019

REFERENCES

Adijanto, J., Du, J., Moffat, C., Seifert, E.L., Hurle, J.B., and Philp, N.J. (2014). The retinal pigment epithelium utilizes fatty acids for ketogenesis. J. Biol. Chem. *289*, 20570–20582.

Agathocleous, M., Meacham, C.E., Burgess, R.J., Piskounova, E., Zhao, Z., Crane, G.M., Cowin, B.L., Bruner, E., Murphy, M.M., Chen, W., et al. (2017). Ascorbate regulates haematopoietic stem cell function and leukaemogenesis. Nature *549*, 476–481.

Arts, J., King, P., Mariën, A., Floren, W., Beliën, A., Janssen, L., Pilatte, I., Roux, B., Decrane, L., Gilissen, R., et al. (2009). JNJ-26481585, a novel "second-generation" oral histone deacetylase inhibitor, shows broad-spectrum preclinical antitumoral activity. Clin. Cancer Res. *15*, 6841–6851.

Barish, G.D., Narkar, V.A., and Evans, R.M. (2006). PPAR delta: a dagger in the heart of the metabolic syndrome. J. Clin. Invest. *116*, 590–597.

Barker, N., van Es, J.H., Kuipers, J., Kujala, P., van den Born, M., Cozijnsen, M., Haegebarth, A., Korving, J., Begthel, H., Peters, P.J., and Clevers, H. (2007). Identification of stem cells in small intestine and colon by marker gene Lgr5. Nature *449*, 1003–1007.

Barker, N., Ridgway, R.A., van Es, J.H., van de Wetering, M., Begthel, H., van den Born, M., Danenberg, E., Clarke, A.R., Sansom, O.J., and Clevers, H. (2009). Crypt stem cells as the cells-of-origin of intestinal cancer. Nature *457*, 608–611.

Beumer, J., and Clevers, H. (2016). Regulation and plasticity of intestinal stem cells during homeostasis and regeneration. Development *143*, 3639–3649.

Beyaz, S., Mana, M.D., Roper, J., Kedrin, D., Saadatpour, A., Hong, S.J., Bauer-Rowe, K.E., Xifaras, M.E., Akkad, A., Arias, E., et al. (2016). High-fat diet enhances stemness and tumorigenicity of intestinal progenitors. Nature *531*, 53–58.

Biton, M., Haber, A.L., Rogel, N., Burgin, G., Beyaz, S., Schnell, A., Ashenberg, O., Su, C.W., Smillie, C., Shekhar, K., et al. (2018). T Helper Cell Cytokines Modulate Intestinal Stem Cell Renewal and Differentiation. Cell *175*, 1307–1320.e22.

Blecher-Gonen, R., Barnett-Itzhaki, Z., Jaitin, D., Amann-Zalcenstein, D., Lara-Astiaso, D., and Amit, I. (2013). High-throughput chromatin immunoprecipitation for genome-wide mapping of in vivo protein-DNA interactions and epigenomic states. Nat. Protoc. *8*, 539–554.

Cimmino, L., Dolgalev, I., Wang, Y., Yoshimi, A., Martin, G.H., Wang, J., Ng, V., Xia, B., Witkowski, M.T., Mitchell-Flack, M., et al. (2017). Restoration of TET2 Function Blocks Aberrant Self-Renewal and Leukemia Progression. Cell *170*, 1079–1095.e20.

Cotter, D.G., Schugar, R.C., and Crawford, P.A. (2013). Ketone body metabolism and cardiovascular disease. Am. J. Physiol. Heart Circ. Physiol. *304*, H1060–H1076.

de la Cruz Bonilla, M., Stemler, K.M., Taniguchi, C.M., and Piwnica-Worms, H. (2018). Stem cell enriched-epithelial spheroid cultures for rapidly assaying small intestinal radioprotectors and radiosensitizers in vitro. Sci. Rep. *8*, 15410.

Degirmenci, B., Valenta, T., Dimitrieva, S., Hausmann, G., and Basler, K. (2018). GLI1-expressing mesenchymal cells form the essential Wnt-secreting niche for colon stem cells. Nature *558*, 449–453.

Dixit, A., Parnas, O., Li, B., Chen, J., Fulco, C.P., Jerby-Arnon, L., Marjanovic, N.D., Dionne, D., Burks, T., Raychowdhury, R., et al. (2016). Perturb-Seq: Dissecting Molecular Circuits with Scalable Single-Cell RNA Profiling of Pooled Genetic Screens. Cell *167*, 1853–1866.e17.

Dobin, A., Davis, C.A., Schlesinger, F., Drenkow, J., Zaleski, C., Jha, S., Batut, P., Chaisson, M., and Gingeras, T.R. (2013). STAR: ultrafast universal RNA-seq aligner. Bioinformatics *29*, 15–21.

Durand, A., Donahue, B., Peignon, G., Letourneur, F., Cagnard, N., Slomianny, C., Perret, C., Shroyer, N.F., and Romagnolo, B. (2012). Functional intestinal stem cells after Paneth cell ablation induced by the loss of transcription factor Math1 (Atoh1). Proc. Natl. Acad. Sci. USA *109*, 8965–8970.

el Marjou, F., Janssen, K.P., Chang, B.H., Li, M., Hindie, V., Chan, L., Louvard, D., Chambon, P., Metzger, D., and Robine, S. (2004). Tissue-specific and inducible Cre-mediated recombination in the gut epithelium. Genesis *39*, 186–193.

Faust, G.G., and Hall, I.M. (2014). SAMBLASTER: fast duplicate marking and structural variant read extraction. Bioinformatics *30*, 2503–2505.

Finak, G., McDavid, A., Yajima, M., Deng, J., Gersuk, V., Shalek, A.K., Slichter, C.K., Miller, H.W., McElrath, M.J., Prlic, M., et al. (2015). MAST: a flexible statistical framework for assessing transcriptional changes and characterizing heterogeneity in single-cell RNA sequencing data. Genome Biol. *16*, 278.

Fre, S., Huyghe, M., Mourikis, P., Robine, S., Louvard, D., and Artavanis-Tsakonas, S. (2005). Notch signals control the fate of immature progenitor cells in the intestine. Nature *435*, 964–968.

Garber, M., Yosef, N., Goren, A., Raychowdhury, R., Thielke, A., Guttman, M., Robinson, J., Minie, B., Chevrier, N., Itzhaki, Z., et al. (2012). A high-throughput chromatin immunoprecipitation approach reveals principles of dynamic gene regulation in mammals. Mol. Cell *47*, 810–822.

Gonneaud, A., Turgeon, N., Boisvert, F.M., Boudreau, F., and Asselin, C. (2015). Loss of histone deacetylase Hdac1 disrupts metabolic processes in intestinal epithelial cells. FEBS Lett. *589* (19 Pt B), 2776–2783.

Guo, J., Longshore, S., Nair, R., and Warner, B.W. (2009). Retinoblastoma protein (pRb), but not p107 or p130, is required for maintenance of enterocyte quiescence and differentiation in small intestine. J. Biol. Chem. *284*, 134–140.

Haber, A.L., Biton, M., Rogel, N., Herbst, R.H., Shekhar, K., Smillie, C., Burgin, G., Delorey, T.M., Howitt, M.R., Katz, Y., et al. (2017). A single-cell survey of the small intestinal epithelium. Nature *551*, 333–339.

Haberland, M., Montgomery, R.L., and Olson, E.N. (2009). The many roles of histone deacetylases in development and physiology: implications for disease and therapy. Nat. Rev. Genet. *10*, 32–42.

Hsieh, J.J., Zhou, S., Chen, L., Young, D.B., and Hayward, S.D. (1999). CIR, a corepressor linking the DNA binding factor CBF1 to the histone deacetylase complex. Proc. Natl. Acad. Sci. USA *96*, 23–28.

Huch, M., Dorrell, C., Boj, S.F., van Es, J.H., Li, V.S., van de Wetering, M., Sato, T., Hamer, K., Sasaki, N., Finegold, M.J., et al. (2013). In vitro expansion of single Lgr5+ liver stem cells induced by Wnt-driven regeneration. Nature *494*, 247–250.

Igarashi, M., and Guarente, L. (2016). mTORC1 and SIRT1 Cooperate to Foster Expansion of Gut Adult Stem Cells during Calorie Restriction. Cell *166*, 436–450.

Ito, K., Carracedo, A., Weiss, D., Arai, F., Ala, U., Avigan, D.E., Schafer, Z.T., Evans, R.M., Suda, T., Lee, C.H., and Pandolfi, P.P. (2012). A PML–PPAR-δ pathway for fatty acid oxidation regulates hematopoietic stem cell maintenance. Nat. Med. *18*, 1350–1358.

Johnson, W.E., Li, C., and Rabinovic, A. (2007). Adjusting batch effects in microarray expression data using empirical Bayes methods. Biostatistics *8*, 118–127.

Kao, H.Y., Ordentlich, P., Koyano-Nakagawa, N., Tang, Z., Downes, M., Kintner, C.R., Evans, R.M., and Kadesch, T. (1998). A histone deacetylase corepressor complex regulates the Notch signal transduction pathway. Genes Dev. *12*, 2269–2277.

Kim, T.H., Escudero, S., and Shivdasani, R.A. (2012). Intact function of Lgr5 receptor-expressing intestinal stem cells in the absence of Paneth cells. Proc. Natl. Acad. Sci. USA *109*, 3932–3937.

Kim, T.H., Li, F., Ferreiro-Neira, I., Ho, L.L., Luyten, A., Nalapareddy, K., Long, H., Verzi, M., and Shivdasani, R.A. (2014). Broadly permissive intestinal chromatin underlies lateral inhibition and cell plasticity. Nature *506*, 511–515.

Kim, T.H., Saadatpour, A., Guo, G., Saxena, M., Cavazza, A., Desai, N., Jadhav, U., Jiang, L., Rivera, M.N., Orkin, S.H., et al. (2016). Single-Cell Transcript Profiles Reveal Multilineage Priming in Early Progenitors Derived from Lgr5(+) Intestinal Stem Cells. Cell Rep. *16*, 2053–2060.

Kowalczyk, M.S., Tirosh, I., Heckl, D., Rao, T.N., Dixit, A., Haas, B.J., Schneider, R.K., Wagers, A.J., Ebert, B.L., and Regev, A. (2015). Single-cell RNA-seq reveals changes in cell cycle and differentiation programs upon aging of hematopoietic stem cells. Genome Res. *25*, 1860–1872.

Langmead, B., Trapnell, C., Pop, M., and Salzberg, S.L. (2009). Ultrafast and memory-efficient alignment of short DNA sequences to the human genome. Genome Biol. *10*, R25.

Leek, J.T., Johnson, W.E., Parker, H.S., Jaffe, A.E., and Storey, J.D. (2012). The sva package for removing batch effects and other unwanted variation in high-throughput experiments. Bioinformatics *28*, 882–883.

Li, B., and Dewey, C.N. (2011). RSEM: accurate transcript quantification from RNA-Seq data with or without a reference genome. BMC Bioinformatics *12*, 323.

Li, J., Ng, E.K., Ng, Y.P., Wong, C.Y., Yu, J., Jin, H., Cheng, V.Y., Go, M.Y., Cheung, P.K., Ebert, M.P., et al. (2009). Identification of retinoic acid-regulated nuclear matrix-associated protein as a novel regulator of gastric cancer. Br. J. Cancer *101*, 691–698.

Lim, J.S., Ibaseta, A., Fischer, M.M., Cancilla, B., O'Young, G., Cristea, S., Luca, V.C., Yang, D., Jahchan, N.S., Hamard, C., et al. (2017). Intratumoural heterogeneity generated by Notch signalling promotes small-cell lung cancer. Nature *545*, 360–364.

Lindemans, C.A., Calafiore, M., Mertelsmann, A.M., O'Connor, M.H., Dudakov, J.A., Jenq, R.R., Velardi, E., Young, L.F., Smith, O.M., Lawrence, G., et al. (2015). Interleukin-22 promotes intestinal-stem-cell-mediated epithelial regeneration. Nature *528*, 560–564.

Liu, T., Ortiz, J.A., Taing, L., Meyer, C.A., Lee, B., Zhang, Y., Shin, H., Wong, S.S., Ma, J., Lei, Y., et al. (2011). Cistrome: an integrative platform for transcriptional regulation studies. Genome Biol. *12*, R83.

McCarthy, D.J., Chen, Y., and Smyth, G.K. (2012). Differential expression analysis of multifactor RNA-Seq experiments with respect to biological variation. Nucleic Acids Res. *40*, 4288–4297.

Metcalfe, C., Kljavin, N.M., Ybarra, R., and de Sauvage, F.J. (2014). Lgr5+ stem cells are indispensable for radiation-induced intestinal regeneration. Cell Stem Cell *14*, 149–159.

Mihaylova, M.M., Sabatini, D.M., and Yilmaz, O.H. (2014). Dietary and metabolic control of stem cell function in physiology and cancer. Cell Stem Cell *14*, 292–305.

Mihaylova, M.M., Cheng, C.W., Cao, A.Q., Tripathi, S., Mana, M.D., Bauer-Rowe, K.E., Abu-Remaileh, M., Clavain, L., Erdemir, A., Lewis, C.A., et al. (2018). Fasting Activates Fatty Acid Oxidation to Enhance Intestinal Stem Cell Function during Homeostasis and Aging. Cell Stem Cell *22*, 769–778.e4.

Muñoz, J., Stange, D.E., Schepers, A.G., van de Wetering, M., Koo, B.K., Itzkovitz, S., Volckmann, R., Kung, K.S., Koster, J., Radulescu, S., et al. (2012). The Lgr5 intestinal stem cell signature: robust expression of proposed quiescent '+4' cell markers. EMBO J. *31*, 3079–3091.

Nakada, D., Levi, B.P., and Morrison, S.J. (2011). Integrating physiological regulation with stem cell and tissue homeostasis. Neuron *70*, 703–718.

Narkar, V.A., Downes, M., Yu, R.T., Embler, E., Wang, Y.X., Banayo, E., Mihaylova, M.M., Nelson, M.C., Zou, Y., Juguilon, H., et al. (2008). AMPK and PPARdelta agonists are exercise mimetics. Cell *134*, 405–415.

Newman, J.C., and Verdin, E. (2017). β-Hydroxybutyrate: A Signaling Metabolite. Annu. Rev. Nutr. *37*, 51–76.

Newman, J.C., Covarrubias, A.J., Zhao, M., Yu, X., Gut, P., Ng, C.P., Huang, Y., Haldar, S., and Verdin, E. (2017). Ketogenic Diet Reduces Midlife Mortality and Improves Memory in Aging Mice. Cell Metab. *26*, 547–557.e8.

Ootani, A., Li, X., Sangiorgi, E., Ho, Q.T., Ueno, H., Toda, S., Sugihara, H., Fujimoto, K., Weissman, I.L., Capecchi, M.R., and Kuo, C.J. (2009). Sustained in vitro intestinal epithelial culture within a Wnt-dependent stem cell niche. Nat. Med. *15*, 701–706.

Oswald, F., Kostezka, U., Astrahantseff, K., Bourteele, S., Dillinger, K., Zechner, U., Ludwig, L., Wilda, M., Hameister, H., Knöchel, W., et al. (2002). SHARP is a novel component of the Notch/RBP-Jkappa signalling pathway. EMBO J. *21*, 5417–5426.

Peregrina, K., Houston, M., Daroqui, C., Dhima, E., Sellers, R.S., and Augenlicht, L.H. (2015). Vitamin D is a determinant of mouse intestinal Lgr5 stem cell functions. Carcinogenesis *36*, 25–31.

Puchalska, P., and Crawford, P.A. (2017). Multi-dimensional Roles of Ketone Bodies in Fuel Metabolism, Signaling, and Therapeutics. Cell Metab. *25*, 262–284.

Qi, Z., Li, Y., Zhao, B., Xu, C., Liu, Y., Li, H., Zhang, B., Wang, X., Yang, X., Xie, W., et al. (2017). BMP restricts stemness of intestinal Lgr5^{+} stem cells by directly suppressing their signature genes. Nat. Commun. *8*, 13824.

Ramírez, F., Ryan, D.P., Grüning, B., Bhardwaj, V., Kilpert, F., Richter, A.S., Heyne, S., Dündar, F., and Manke, T. (2016). deepTools2: a next generation web server for deep-sequencing data analysis. Nucleic Acids Res. *44* (W1), W160-5.

Rickelt, S., and Hynes, R.O. (2018). Antibodies and methods for immunohistochemistry of extracellular matrix proteins. Matrix Biol. *71-72*, 10–27.

Rodríguez-Colman, M.J., Schewe, M., Meerlo, M., Stigter, E., Gerrits, J., Pras-Raves, M., Sacchetti, A., Hornsveld, M., Oost, K.C., Snippert, H.J., et al. (2017). Interplay between metabolic identities in the intestinal crypt supports stem cell function. Nature *543*, 424–427.

Rognstad, R. (1979). Rate-limiting steps in metabolic pathways. J. Biol. Chem. *254*, 1875–1878.

Sancho, R., Cremona, C.A., and Behrens, A. (2015). Stem cell and progenitor fate in the mammalian intestine: Notch and lateral inhibition in homeostasis and disease. EMBO Rep. *16*, 571–581.

Sasaki, N., Sachs, N., Wiebrands, K., Ellenbroek, S.I., Fumagalli, A., Lyubimova, A., Begthel, H., van den Born, M., van Es, J.H., Karthaus, W.R., et al. (2016). Reg4+ deep crypt secretory cells function as epithelial niche for Lgr5+ stem cells in colon. Proc. Natl. Acad. Sci. USA *113*, E5399–E5407.

Sato, T., Vries, R.G., Snippert, H.J., van de Wetering, M., Barker, N., Stange, D.E., van Es, J.H., Abo, A., Kujala, P., Peters, P.J., and Clevers, H. (2009). Single Lgr5 stem cells build crypt-villus structures in vitro without a mesenchymal niche. Nature *459*, 262–265.

Sato, T., van Es, J.H., Snippert, H.J., Stange, D.E., Vries, R.G., van den Born, M., Barker, N., Shroyer, N.F., van de Wetering, M., and Clevers, H. (2011). Paneth cells constitute the niche for Lgr5 stem cells in intestinal crypts. Nature *469*, 415–418.

Shimazu, T., Hirschey, M.D., Newman, J., He, W., Shirakawa, K., Le Moan, N., Grueter, C.A., Lim, H., Saunders, L.R., Stevens, R.D., et al. (2013). Suppression of oxidative stress by β-hydroxybutyrate, an endogenous histone deacetylase inhibitor. Science *339*, 211–214.

Shoshkes-Carmel, M., Wang, Y.J., Wangensteen, K.J., Tóth, B., Kondo, A., Massasa, E.E., Itzkovitz, S., and Kaestner, K.H. (2018). Author Correction: Subepithelial telocytes are an important source of Wnts that supports intestinal crypts. Nature *560*, E29.

Shroyer, N.F., Helmrath, M.A., Wang, V.Y., Antalffy, B., Henning, S.J., and Zoghbi, H.Y. (2007). Intestine-specific ablation of mouse atonal homolog 1 (Math1) reveals a role in cellular homeostasis. Gastroenterology *132*, 2478–2488.

Skarnes, W.C., Rosen, B., West, A.P., Koutsourakis, M., Bushell, W., Iyer, V., Mujica, A.O., Thomas, M., Harrow, J., Cox, T., et al. (2011). A conditional knockout resource for the genome-wide study of mouse gene function. Nature *474*, 337–342.

Subramanian, A., Tamayo, P., Mootha, V.K., Mukherjee, S., Ebert, B.L., Gillette, M.A., Paulovich, A., Pomeroy, S.L., Golub, T.R., Lander, E.S., and Mesirov, J.P. (2005). Gene set enrichment analysis: a knowledge-based approach for interpreting genome-wide expression profiles. Proc. Natl. Acad. Sci. USA *102*, 15545–15550.

Tian, H., Biehs, B., Chiu, C., Siebel, C.W., Wu, Y., Costa, M., de Sauvage, F.J., and Klein, O.D. (2015). Opposing activities of Notch and Wnt signaling regulate intestinal stem cells and gut homeostasis. Cell Rep. *11*, 33–42.

Tinkum, K.L., Stemler, K.M., White, L.S., Loza, A.J., Jeter-Jones, S., Michalski, B.M., Kuzmicki, C., Pless, R., Stappenbeck, T.S., Piwnica-Worms, D., and Piwnica-Worms, H. (2015). Fasting protects mice from lethal DNA damage by promoting small intestinal epithelial stem cell survival. Proc. Natl. Acad. Sci. USA *112*, E7148–E7154.

van der Flier, L.G., van Gijn, M.E., Hatzis, P., Kujala, P., Haegebarth, A., Stange, D.E., Begthel, H., van den Born, M., Guryev, V., Oving, I., et al. (2009). Transcription factor achaete scute-like 2 controls intestinal stem cell fate. Cell *136*, 903–912.

VanDussen, K.L., Carulli, A.J., Keeley, T.M., Patel, S.R., Puthoff, B.J., Magness, S.T., Tran, I.T., Maillard, I., Siebel, C., Kolterud, Å., et al. (2012). Notch signaling modulates proliferation and differentiation of intestinal crypt base columnar stem cells. Development *139*, 488–497.

Vooijs, M., Liu, Z., and Kopan, R. (2011). Notch: architect, landscaper, and guardian of the intestine. Gastroenterology *141*, 448–459.

Wang, Q., Zhou, Y., Rychahou, P., Fan, T.W., Lane, A.N., Weiss, H.L., and Evers, B.M. (2017). Ketogenesis contributes to intestinal cell differentiation. Cell Death Differ. *24*, 458–468.

Wang, B., Rong, X., Palladino, E.N.D., Wang, J., Fogelman, A.M., Martin, M.G., Alrefai, W.A., Ford, D.A., and Tontonoz, P. (2018). Phospholipid Remodeling and Cholesterol Availability Regulate Intestinal Stemness and Tumorigenesis. Cell Stem Cell *22*, 206–220.e4.

Yamaguchi, M., Tonou-Fujimori, N., Komori, A., Maeda, R., Nojima, Y., Li, H., Okamoto, H., and Masai, I. (2005). Histone deacetylase 1 regulates retinal neurogenesis in zebrafish by suppressing Wnt and Notch signaling pathways. Development *132*, 3027–3043.

Yan, K.S., Janda, C.Y., Chang, J., Zheng, G.X.Y., Larkin, K.A., Luca, V.C., Chia, L.A., Mah, A.T., Han, A., Terry, J.M., et al. (2017). Non-equivalence of Wnt and R-spondin ligands during Lgr5^{+} intestinal stem-cell self-renewal. Nature *545*, 238–242.

Yang, Q., Bermingham, N.A., Finegold, M.J., and Zoghbi, H.Y. (2001). Requirement of Math1 for secretory cell lineage commitment in the mouse intestine. Science *294*, 2155–2158.

Yilmaz, O.H., Katajisto, P., Lamming, D.W., Gültekin, Y., Bauer-Rowe, K.E., Sengupta, S., Birsoy, K., Dursun, A., Yilmaz, V.O., Selig, M., et al. (2012). mTORC1 in the Paneth cell niche couples intestinal stem-cell function to calorie intake. Nature *486*, 490–495.

Yin, X., Farin, H.F., van Es, J.H., Clevers, H., Langer, R., and Karp, J.M. (2014). Niche-independent high-purity cultures of Lgr5+ intestinal stem cells and their progeny. Nat. Methods *11*, 106–112.

Zecchini, V., Domaschenz, R., Winton, D., and Jones, P. (2005). Notch signaling regulates the differentiation of post-mitotic intestinal epithelial cells. Genes Dev. *19*, 1686–1691.

Zhang, M., Behbod, F., Atkinson, R.L., Landis, M.D., Kittrell, F., Edwards, D., Medina, D., Tsimelzon, A., Hilsenbeck, S., Green, J.E., et al. (2008). Identification of tumor-initiating cells in a p53-null mouse model of breast cancer. Cancer Res. *68*, 4674–4682.

Zhao, M., Chen, X., Gao, G., Tao, L., and Wei, L. (2009). RLEdb: a database of rate-limiting enzymes and their regulation in human, rat, mouse, yeast and E. coli. Cell Res. *19*, 793–795.

Zimberlin, C.D., Lancini, C., Sno, R., Rosekrans, S.L., McLean, C.M., Vlaming, H., van den Brink, G.R., Bots, M., Medema, J.P., and Dannenberg, J.H. (2015). HDAC1 and HDAC2 collectively regulate intestinal stem cell homeostasis. FASEB J. *29*, 2070–2080.

STAR★METHODS

KEY RESOURCES TABLE

REAGENT or RESOURCE	SOURCE	IDENTIFIER
Antibodies		
rabbit anti-HMGCS2	Abcam	ab137043;RRID:AB_2749817
rat anti-BrdU	Abcam	ab6326;RRID:AB_2313786
rabbit monoclonal anti-OLFM4	CST	clone PP7
rabbit polyclonal anti-Lysozyme	Thermo	RB-372-A; RRID:AB_138388
rabbit anti-chromogranin A	Abcam	ab15160; RRID:AB_301704
rabbit Cleaved Caspase-3	CST	#9664; RRID:AB_2070042
rabbit polyclonal anti-RFP	Rockland	600-401-379; RRID:AB_2209751
goat polyclonal anti-Chromogranin A	Santa Cruz	sc-1488; RRID:AB_2276319
anti-HMGCS2	Sigma	AV41562; RRID:AB_1850800
rabbit anti-Cleaved Notch1	CST	#4147; RRID:AB_2153348
rabbit anti-H3K27ac	CST	#8173; RRID:AB_10949503
Rabbit anti-HDAC1 antibody	Abcam	ab53091; RRID:AB_2264059
Chemicals, Peptides, and Recombinant Proteins		
Matrigel™	Corning	356231
Advanced DMEM	GIBCO	12491015
DMEM/F12	GIBCO	11320033
SMEM	Life Technologies	11380-037
Murine EGF	PeproTech	315-09
Recombinant Murine Noggin	PeproTech	250-38
R-spondin	Sino Biological	50316-M08S
N-acetyl-L-cysteine	Sigma-Aldrich	A9165
N2	Life Technologies	17502001
B27	Life Technologies	17504044
Chir99021	LC Laboratories	04-0004
Y-27632	ApexBio	A3008
JAG-1 protein	AnaSpec	AS-61298
Sodium beta-hydroxybutyrate	Sigma	54965
Quisinosta (JNJ-26481585) 2HCl	Selleckchem	S1096
Entinostat (MS-275)	Selleckchem	S1053
Trichostatin A	Selleckchem	S1045
γ-secretase inhibitor MK-0752	Cayman Chemical Company	471905-41-6
^{13}C-Palmitate	Sigma	605573
PLGA encapsulated βOHB	This paper	N/A
βOHB oligomers	This paper	N/A
Critical Commercial Assays		
RNAscope 2.0 HD Detection Kit	ACD RNAscope®	
RNAscope probe: *Mm-Hmgcs2*	ACD RNAscope®	Ref#437141
RNAscope probe: *Mm-Hes1*	ACD RNAscope®	Ref#417701
RNAscope probe*: Mm- Atoh1*	ACD RNAscope®	Ref#408791
RNAscope probe*: Mm-Lgr5*	ACD RNAscope®	Ref#312171
β-Hydroxybutyrate (Ketone Body) Colorimetric Assay Kit	Cayman	#700190

(*Continued on next page*)

Continued

REAGENT or RESOURCE	SOURCE	IDENTIFIER
TSA Alexa Fluor 488 tyramide signal amplification kit	Life Technologies	T20948
Deposited Data		
Population RNA sequencing data I	GEO	GSE89568 https://www.ncbi.nlm.nih.gov/geo/query/acc.cgi?acc=GSE89568
Population RNA sequencing data II	GEO	GSE67324 https://www.ncbi.nlm.nih.gov/geo/query/acc.cgi?acc=GSE67324
Single-cell RNA-seq data	GEO	GSE112205 https://www.ncbi.nlm.nih.gov/geo/query/acc.cgi?acc=GSE112205
ChIP-seq H3K27ac data	GEO	GSE134044 https://www.ncbi.nlm.nih.gov/geo/query/acc.cgi?acc=GSE134044
Experimental Models: Cell Lines		
Hes1-GFP organoid	This paper	N/A
NICD-GFP^{LSL} organoid	This paper	N/A
Experimental Models: Organisms/Strains		
Lgr5-CreERT2	Clevers Lab	https://www.ncbi.nlm.nih.gov/pmc/articles/PMC3634804/
Villin-CreERT2	el Marjou et al., 2004	N/A
Hmgcs2-lacZ reporter	This paper	RRID:IMSR_KOMP:CSD37366-1e-Wtsi
Hmgcs2 $^{loxp/loxp}$; *Lgr5-eGFP-IRES-CreERT2*	This paper	N/A
Hmgcs2 $^{loxp/loxp}$; *Lgr5-CreERT2; tdTomato*^{LSL}	This paper	N/A
Hmgcs2 $^{loxp/loxp}$; Villin-CreERT2	This paper	N/A
Atoh1(*Math1*)$^{loxp/loxp}$;Villin-CreERT2	Shivdasani Lab	https://www.ncbi.nlm.nih.gov/pmc/articles/PMC4151315/
Hes1-GFP	Sage Lab	https://www.ncbi.nlm.nih.gov/pmc/articles/PMC5776014/
Rosa^{N1-IC}	Jackson Laboratory	#008159; https://www.jax.org/strain/008159 RRID:IMSR_JAX:008159
Oligonucleotides		
Genotyping primer:Hmgcs2WT(R):CCTGTGAG ACAAACCTTTGGG	IDT	N/A
Genotyping primer:Hmgcs2tg(R):GACCTTGGG ACCACCTCATC		
Genotyping primer:Hmgcs2Comm(F):TTACCA TGGTGGGGAAGTCA		
Hmgcs2 excision confirmation primer: Loxp Cre (F):GTTTACCATGGTGGGGAAGTC	IDT	N/A
Hmgcs2 excision confirmation primer: LoxpComm(R):CCTCCCTTTCCTAAGTTGCTC		
qPCR primers for Hmgcs2:Hmgcs2 (F):ATACC ACCAACGCCTGTTATGG	IDT	N/A
qPCR primers for Hmgcs2:Hmgcs2 (R):CAAT GTCACCACAGACCACCAG	IDT	N/A
Recombinant DNA		
Hdac1 CRISPR-deletion	Santa Cruz Biotechnology, Inc	sc-436647
Cre-expression	Santa Cruz Biotechnology, Inc	sc-418923
Cre-expression and *Hmgcs2* CRISPR-deletion	this paper; VectorBuilder	VB180615-1103 gue
Software and Algorithms		
GraphPad Prism 7	GraphPad Software, Inc.	https://www.graphpad.com/
FlowJo	TreeStar	https://www.flowjo.com/solutions/flowjo/downloads

(*Continued on next page*)

Continued		
REAGENT or RESOURCE	SOURCE	IDENTIFIER
10x Cellranger	10X Genomics Version 1.3.1	https://support.10xgenomics.com/single-cell-gene-expression/software/pipelines/latest/what-is-cell-ranger
Gene Set Enrichment Analysis (GSEA)	GSEA software	http://software.broadinstitute.org/gsea/index.jsp RRID:SCR_003199
RSEM	Li and Dewey, 2011	http://deweylab.github.io/RSEM/
R code for single-cell RNA-seq analysis	Haber et al., 2017	https://github.com/adamh-broad/single_cell_intestine
Other		
Ketogenic diet (KTD)	Research diet, Inc.	D0604601

LEAD CONTACT AND MATERIALS AVAILABILITY

Further information and requests for resources and reagents should be directed to and will be fulfilled by the Lead Contact, Ömer H. Yilmaz (ohyilmaz@mit.edu).

EXPERIMENTAL MODEL AND SUBJECT DETAILS

Animal

Mouse strains

Hmgcs2-lacZ reporter and conditional loxp mice were generated using a knockout-first strategy(Skarnes et al., 2011) to functionally validate whether *Hmgcs2*-expressing cells harbor function ISC activity and whether *Hmgcs2* is necessary for ISC maintenance. The knockout-first combines the advantage of both a reporter-tagged and a conditional mutation. Briefly, a cassette containing mouse En2 splicing acceptor (SA), lacZ, and promoter-driven neomycin resistant gene (Neo) is inserted in introns of target genes. The initial allele (*Hmgcs2*-Vector, V)(KOMP: PG00052_Z_4_A06) is predicted to generate a null allele through splicing to the lacZ trapping element. Targeted clones therefore report endogenous gene expression and carry null mutation (Figures 2A and S2A). Successful targeting was validated by Southern blotting (Figure S1G) and PCR analysis (Figure S2B). Conditional alleles (*Hmgcs2-loxp*) can be generated by removal of the gene trap cassette using Flp recombinase. To investigate the necessity of Hmgcs2 in maintaining ISC functions, we generated *Hmgcs2*$^{loxp/loxp}$ mice and crossed them to *Lgr5-eGFP-IRES-CreERT2*(Barker et al., 2007) and to *Lgr5-CreERT2; tdTomato*^{LSL} (Huch et al., 2013) reporter mice separately. CRE-mediated excisions in sorted GFP+ cells and in tdTomato+ crypt cells were both confirmed by PCR (Figures S2B and S2F). *Lgr5-CreERT2; tdTomato*^{LSL} were generated by crossing *Lgr5-IRES-CreERT2* mice (a gift from Dr. Hans Clevers)(Huch et al., 2013) to tdTomatoLSL mice (Jackson Laboratory, #007909). *Hmgcs2*$^{loxp/loxp}$;*Villin-CreERT2* mice were generated by crossing *Hmgcs2*$^{loxp/loxp}$ mice to *Villin-CreERT2* mice (el Marjou et al., 2004). *Atoh1*(*Math1*)$^{loxp/loxp}$;*Villin-CreERT2* mice were generated by crossing *Atoh1*(*Math1*)$^{loxp/loxp}$ mice to *Villin-CreERT2* mice (Shroyer et al., 2007). Hes1-GFP reporter mice were previously described (Lim et al., 2017). In this study, both male and female mice were used at the ages of 3-5 months unless otherwise specified in the figure legends.

Organoids

Hes1-GFP organoids were generated from adult male and female Hes1-GFP reporter mice (Lim et al., 2017). Primary NICD-GFP^{LSL} organoids were generated from adult male Rosa$^{N1\text{-}IC}$ mice (Jackson Laboratory, #008159). Primary organoids were cultured in the CO2 incubator (37°C, 5% CO2) using the complete crypt culture medium, as described in Crypt Isolation and Culturing)(Mihaylova et al., 2018).

Human intestinal samples

Human duodenal biopsies that were diagnosed as normal were obtained from 10 patients (n = 4 19-to-20-year-old females, n = 3 81-to-84-year-old females and n = 3 19-to-20-year-old males). The Massachusetts General Hospital (MGH) Institutional Review Board committee approved the study protocol.

METHOD DETAILS

In vivo treatments

Tamoxifen treatment

Tamoxifen injections were achieved by intraperitoneal (i.p.) tamoxifen injection suspended in sunflower seed oil (Spectrum S1929) at a concentration of 10 mg/ml, 250ul per 25 g of body weight, and administered at the time points indicated in figures and figure leg-

ends. *Irradiation experiments*. Mice were challenged by a lethal dose of irradiation (7.5Gy x 2, 6 hours apart). Intestine tissues were collected for histology 5 days after ionizing irradiation-induced (XRT). Exogenous *βOHB* treatments: Mice received a single oral dose of βOHB-encapsulated PLGA nanoparticles (16.67mg/25 g in 500ul) or *βOHB* oligomers (15mg/25 g in 500ul) 16hrs prior to irradiation. See also Supplemental Methods for preparation of *βOHB* nanoparticles and oligomers. *HDAC inhibitor treatments*. Mice received up to 5 injections (i.p.) of vehicle (2% DMSO+30% PEG 300+ddH2O) or Quisinostat (JNJ-26481585) 2HCl (1 mg/kg per injection). *Ketogenic diet (KTD)*. Per-calorie macronutrient content: 15 kcal protein, 5 kcal carbohydrate and 80 kcal fat per 100 kcal KTD (Research diet, Inc. D0604601). See also supplement Table S4 for the ingredient composition. Food was provided *ad libitum* at all times. The fat sources are Crisco, cocoa butter, and corn oil. *Glucose solution*. Glucose supplement was prepared by adding 13 g D-(+)-Glucose (Sigma, Cat. #G8270) into 100 mL drinking water of mice. Unless otherwise specified in figure legends, all experiments involving mice were carried out using adult male and female mice ($n > 3$ per group), with approval from the Committee for Animal Care at MIT and under supervision of the Department of Comparative Medicine at MIT. See also Quantification and Statistical Analysis for general information related to experimental design.

Beta-Hydroxybutyrate (βOHB) measurements

Serum βOHB

Blood was obtained via submandibular vein bleed (10-40 uL). Blood was collected into an eppendorf tube and allowed to clot for 15–30 minutes at room temperature. Serum was separated by centrifugation at 1500 x g for 15 min at 4°C. Serum samples were frozen at −80°C until thawed for assay. *Crypts βOHB*. Intestinal crypts freshly isolated in PBS were aliquoted into two samples. Samples were pelleted (centrifuged at 300 x g for 5 minutes) and re-suspended in lysis buffer of BCA assay (Thermofisher, # 23225) for measuring total proteins and that for Beta-Hydroxybutyrate measurements (Cayman, #700190). Level of crypts βOHB was normalized to total proteins of each sample.

Crypt Isolation and culturing

As previously reported and briefly summarized here (Mihaylova et al., 2018), small intestines were removed, washed with cold PBS, opened longitudinally and then incubated on ice with PBS plus EDTA (10 mM) for 30-45 min. Tissues were then moved to PBS. Crypts were then mechanically separated from the connective tissue by shaking or by scraping, and then filtered through a 70-μm mesh into a 50 mL conical tube to remove villus material and tissue fragments. Isolated crypts for cultures were counted and embedded in Matrigel (Corning 356231 growth factor reduced) at 5-10 crypts per μl and cultured in a modified form of medium as described previously (Sato et al., 2009; Yilmaz et al., 2012). Unless otherwise noted, crypt culture media consists of Advanced DMEM (GIBCO) that was supplemented with EGF 40 ng ml^{-1} (PeproTech), Noggin 200 ng ml^{-1} (PeproTech), R-spondin 500 ng ml^{-1} (R&D, Sino Bioscience or (Ootani et al., 2009)), *N*-acetyl-L-cysteine 1 μM (Sigma-Aldrich), N2 1X (Life Technologies), B27 1X (Life Technologies), CHIR99021 3 μM (LC laboratories), and Y-27632 dihydrochloride monohydrate 10uM (Sigma-Aldrich). Intestinal crypts were cultured in the above mentioned media in 20-25 μL droplets of Matrigel were plated onto a flat bottom 48-well plate (Corning 3548) and allowed to solidify for 20-30 minutes in a 37°C incubator. Three hundred microliters of crypt culture medium was then overlaid onto the Matrigel™, changed every three days, and maintained at 37°C in fully humidified chambers containing 5% CO_2. Clonogenicity (colony-forming efficiency) was calculated by plating 50–300 crypts and assessing organoid formation 3-7 days or as specified after initiation of cultures. Beta-hydroxybutyrate (Sigma, 54965), Quisinostat (JNJ-26481585) 2HCl (Selleckchem, S1096), Entinostat (MS-275) (Selleckchem, S1053), Trichostatin A (Selleckchem, S1045) and γ-secretase inhibitor MK-0752 (Cayman Chemical Company, 471905-41-6) were added into cultures as indicated in the figure legends. Plasmids for *Hdac1* CRISPR-deletion (sc-436647), Cre-expression (sc-418923), Cre-expression and *Hmgcs2* CRISPR-deletion (VB180615-1103 gue) were used for organoid transfection according to manufacturers' instructions.

If not directly used for cultures, crypts were then dissociated into single cells and sorted by flowcytometry. Isolated ISCs or progenitor cells were centrifuged at 300 g for 5 minutes, re-suspended in the appropriate volume of crypt culture medium and seeded onto 20-25 μL Matrigel (Corning 356231 growth factor reduced) containing 1 μM JAG-1 protein (AnaSpec, AS-61298) in a flat bottom 48-well plate (Corning 3548). Alternatively, ISCs and Paneth cells were mixed after sorting in a 1:1 ratio, centrifuged (300g, 5min), and then seeded onto Matrigel. The Matrigel and cells were allowed to solidify before adding 300 μL of crypt culture medium. The crypt media was changed every third day.

RT-PCR and *In Situ* Hybridization (ISH)

25,000 cells were sorted into Tri Reagent (Life Technologies), and total RNA was purified according to the manufacturer's instructions with following modification: the aqueous phase containing total RNA was purified using RNeasy plus kit (QIAGEN). RNA was converted to cDNA with cDNA synthesis kit (Bio-Rad). qRT-PCR was performed with diluted cDNA (1:5) in 3 wells for each primer and SYBR green master mix on Roche LightCycler® 480 detection system. Primers used are previously described[6]. Single-molecule *in situ* hybridization was performed using Advanced Cell Diagnostics RNAscope 2.0 HD Detection Kit (Fast Red dye) for the following probes: *Mm-Hmgcs2, Mm-Hes1, Mm- Atoh1. Mm-Lgr5.* For IHC and ISH co-staining, after signal detection of *Lgr5* ISH, slides were dried and proceeded with regular IHC for HMGCS2 staining.

Immunostaining and Immunoblotting

As previously described (Beyaz et al., 2016; Rickelt and Hynes, 2018; Yilmaz et al., 2012), tissues were fixed in 10% formalin, paraffin embedded and sectioned. Antigen retrieval was performed with Borg Decloaker RTU solution (Biocare Medical) in a pressurized Decloaking Chamber (Biocare Medical) for 3 minutes. *Antibodies used for immunohistochemistry*: rabbit anti-HMGCS2 (1:500, Abcam ab137043), rat anti-BrdU (1:2000, Abcam 6326), rabbit monoclonal anti-OLFM4 (1:10,000, gift from CST, clone PP7), rabbit polyclonal anti-lysozyme (1:250, Thermo RB-372-A1), rabbit anti-chromogranin A (1:4,000, Abcam 15160), rabbit Cleaved Caspase-3 (1:500, CST #9664), rabbit polyclonal anti-RFP (1:500, Rockland 600-401-379), goat polyclonal anti-Chromogranin A (1:100, Santa Cruz sc-1488). Biotin-conjugated secondary donkey anti-rabbit or anti-rat antibodies were used from Jackson ImmunoResearch. The Vectastain Elite ABC immunoperoxidase detection kit (Vector Labs PK-6101) followed by Dako Liquid DAB+ Substrate (Dako) was used for visualization. *Antibodies used for immunofluorescence*: tdTomato and Lysozyme immunofluorescence costaining, Alexa Fluor 488 and 568 secondary antibody (Invitrogen). For NICD and H3K27ac staining, antibodies rabbit anti-Cleaved Notch1 (CST, #4147), rabbit anti-H3K27ac (CST,#8173) and TSA Alexa Fluor 488 tyramide signal amplification kit (Life Technologies, T20948) was used. Slides were stained with DAPI (2 μg/mL) for 1 min and covered with Prolong Gold (Life Technologies) mounting media. All antibody incubations involving tissue or sorted cells were performed with Common Antibody Diluent (Biogenex). The following antibodies were used for western blotting: anti-HMGCS2 (1:500, Sigma AV41562) and anti- alpha tubulin (1:3000, Santa Cruz sc- 8035). Single cell western blotting was performed using Proteinsimple Milo system according to manufacturer's instructions. Anti-HDAC1 antibody (1:200, ab53091) was used to detect HDAC1 levels by flow cytometry and analyzed using FlowJo.

13C-Palmitate labeling and LC/MS Methods

13C-Palmitate labeling assay were performed as previously described in (Mihaylova et al., 2018). Briefly, intestinal crypts were isolated from mice and incubated in RPMI media containing above mentioned crypt components and 30mM 13C-Palmitate for 60 minutes and metabolites were extracted for LC/MS analysis.

Population RNA-Seq analysis

Reads were aligned against the mm10 murine genome assembly, with ENSEMBL 88 annotation, using v. STAR 2.5.3a, with flags–runThreadN 8–runMode alignReads–outFilterType BySJout–outFilterMultimapNmax 20–alignSJoverhangMin 8–alignSJDBoverhangMin 1–outFilterMismatchNmax 999–alignIntronMin 10–alignIntronMax 1000000–alignMatesGapMax 1000000–outSAMtype BAM SortedByCoordinate–quantMode TranscriptomeSAM pointing to a 75nt-junction STAR genome suffix array(Dobin et al., 2013). Quantification was performed using RSEM with flags–forward-prob 0–calc-pme–alignments -p 8(Li and Dewey, 2011). The resulting posterior mean estimates of read counts were retrieved and used for differential expression analysis using the edgeR package, in the R 3.4.0 statistical framework(McCarthy et al., 2012). In the absence of replicates, pairwise comparisons of samples/conditions were performed using an exact test with a dispersion set to bcv-squared, where bcv value was set to 0.3. For pooled analyses (with samples pooled by their ISC, Progenitor or Paneth cell status), exact tests were similarly performed, with dispersions estimated from the data using the estimateDisp function. Benjamini-Hochberg adjusted p values and log2-fold-changes were retrieved and used for downstream analyses.

GSEA analysis of bulk RNA-Seq

The command-line version of the GSEA tool(Subramanian et al., 2005) was used to analyze potential enrichment of interesting gene sets affected by age, diet, etc. Genes were ranked according to their log2(FoldChange) values and analyzed using the ''pre-ranked'' mode of the GSEA software using the following parameters: -norm meandiv -nperm 5000 -scoring_scheme weighted -set_max 2000 -set_min 1 -rnd_seed timestamp. The MSigDB C2 collection was analyzed and the c2_REACTOME_SIGNALING_BY_NOTCH.gmt dataset was plotted using GSEA.

Droplet scRNA-seq

Cells were sorted with the same parameters as described above for flow-cytometry into into an Eppendorf tube containing 50μl of 0.4% BSA-PBS and stored on ice until proceeding to the Chromium Single Cell Platform. Single cells were processed through the Chromium Single Cell Platform using the Chromium Single Cell 3′ Library, Gel Bead and Chip Kits (10X Genomics, Pleasanton, CA), following the manufacturer's protocol. Briefly, an input of 7,000 cells was added to each channel of a chip with a recovery rate of 1,500-2,500 cells. The cells were then partitioned into Gel Beads in Emulsion (GEMs) in the Chromium instrument, where cell lysis and barcoded reverse transcription of RNA occurred, followed by amplification, tagmentation and 5′ adaptor attachment. Libraries were sequenced on an Illumina NextSeq 500.

Droplet scRNA-seq data processing

Alignment to the mm10 mouse genome and unique molecular identifier (UMI) collapsing was performing using the Cellranger toolkit (version 1.3.1, 10X Genomics). For each cell, we quantified the number of genes for which at least one UMI was mapped, and then excluded all cells with fewer than 1,000 detected genes. We then identified highly variable genes. *Variable gene selection*. A logistic regression was fit to the cellular detection fraction (often referred to as α), using the total number of UMIs per cell as a predictor. Outliers from this curve are genes that are expressed in a lower fraction of cells than would be expected given the total number

of UMIs mapping to that gene, i.e., cell-type- or state-specific genes. We controlled for mouse-to-mouse variation by providing mouse labels as a covariate and selecting only genes that were significant in all mice, and used a threshold of deviance < −0.1, producing a set of 806 variable genes. Known cell-cycle genes (either part of a cell-cycle signature(Kowalczyk et al., 2015) or in the Gene Ontology term 'Cell-Cycle': GO:0007049) were excluded, resulting in a set of 672 variable genes. *Dimensionality reduction.* We restricted the expression matrix to the subsets of variable genes and high-quality cells noted above, and then centered and scaled values before inputting them into principal component analysis (PCA), which was implemented using the R package 'Seurat' version 2.3.4. Given that many principal components explain very little of the variance, the signal-to-noise ratio can be improved substantially by selecting a subset of n top principal components, we selected 13 principal components by inspection of the 'knee' in a scree plot. Scores from only these principal components were used as the input to further analysis. *Batch correction and clustering.* Both prior knowledge and our data show that different cell types have differing proportions in the small intestine. This makes conventional batch correction difficult, as, due to random sampling effects, some batches may have very few of the rarest cells. To avoid this problem, we performed an initial round of unsupervised clustering using *k*-nearest neighbor (*k*NN) graph-based clustering, implemented in Seurat using the 'FindClusters' function, using a resolution parameter of 1. We next performed batch correction within each identified cluster (which contained only transcriptionally similar cells) ameliorating problems with differences in abundance. Batch correction was performed (only on the 672 variable genes) using ComBat(Johnson et al., 2007) as implemented in the R package sva(Leek et al., 2012) using the default parametric adjustment mode. Following this batch correction step, we re-ran PCA and *k*NN-based clustering to identify the final clusters (resolution parameter = 0.25). *Visualization*. For visualization, the dimensionality of the datasets was further reduced using the 'Barnes-hut' approximate version of t-SNE(Haber et al., 2017) (http://jmlr.org/papers/v15/vandermaaten14a.html) as implemented in the Rtsne function from the 'Rtsne' R package using 1,000 iterations and a perplexity setting of 60. *Testing for changes in cell-type proportions.* To assess the significance of changes in the proportions of cells in different clusters, we used a negative binomial regression model to model the counts of cells in each cluster, while controlling for any mouse-to-mouse variability among our biological replicates. For each cluster, we model the number of cells detected in each analyzed mouse as a random count variable using a negative binomial distribution. The frequency of detection is then modeled by using the natural log of the total number of cells profiled in a given mouse as an offset. The condition of each mouse (i.e., knock-out or wild-type) is then provided as a covariate. The negative binomial model was fit using the R command 'glm.nb' from the 'MASS' package. The *p-value* for the significance of the effect produced by the knock-out was then assessed using a likelihood-ratio test, computing using the R function 'anova'. *Scoring cells using signature gene sets.* To obtain a score for a specific set of *n* genes in a given cell, a 'background' gene set was defined to control for differences in sequencing coverage and library complexity. The background gene set was selected to be similar to the genes of interest in terms of expression level. Specifically, the 10*n* nearest neighbors in the 2-D space defined by mean expression and detection frequency across all cells were selected. The signature score for that cell was then defined as the mean expression of the *n* signature genes in that cell, minus the mean expression of the 10*n* background genes in that cell. Violin plots to visualize the distribution of these scores were generated using the R package 'ggplot2′. We scored cells in this manner for Paneth cell markers(Haber et al., 2017), proliferation(Kowalczyk et al., 2015), apoptosis(Dixit et al., 2016), and intestinal stem cell markers(Muñoz et al., 2012). *Enrichment analysis.* Enrichment analysis was performed using the hypergeometric probability computed in R using 'phyper'. *Differential expression and cell-type signatures.* To identify maximally specific genes for cell-types, we performed differential expression tests between each pair of clusters for all possible pairwise comparisons. Then, for a given cluster, putative signature genes were filtered using the maximum FDR Q-value and ranked by the minimum $\log_2$ fold-change of means (across the comparisons). This is a stringent criterion because the minimum fold-change and maximum Q-value represent the weakest effect-size across all pairwise comparisons. Cell-type signature genes for the initial droplet based scRNA-seq data were obtained using a maximum FDR of 0.001 and a minimum $\log_2$ fold-change of 0.1. Differential expression tests were carried using a two part 'hurdle' model to control for both technical quality and mouse-to-mouse variation. This was implemented using the R package MAST(Finak et al., 2015), and p values for differential expression were computed using the likelihood-ratio test. Multiple hypothesis testing correction was performed by controlling the false discovery rate (FDR) using the R function 'p.adjust', and results were visualized using 'volcano' plots constructed using 'ggplot2′. *Code availability.* R scripts enabling the main steps of the analysis to be reproduced are available from the corresponding authors upon request.

ChIP-sequencing analysis

Small intestine crypt isolation

Crypt isolation followed previously published protocols with minor modifications (Guo et al., 2009; Tinkum et al., 2015). Briefly fed or fasted mice were euthanized by CO2, the whole SI was collected, flushed with PBS (Ca^{2+}- and Mg^{2+}-free, 2mM EDTA, 100 nM TSA) to remove feces, and the mesentery was removed. The SI sample was cut longitudinally then cut transversely into 4 equal pieces. Each sample was placed on ice in PBS (Ca^{2+}- and Mg^{2+}-free, 100nM TSA) while the remaining samples were collected. After collection of all samples, SI were incubated in PBS (Ca^{2+}- and Mg^{2+}-free, 2 mM EDTA, 100 nM TSA) for 10 min then transferred to HBSS (Ca^{2+}- and Mg^{2+}-free, 2 mM EDTA, 100 nM TSA). Crypts were released through a series of vortex washes at 1,600rpm in HBSS (Ca^{2+}- and Mg^{2+}-free, 2 mM EDTA, 100 nM TSA) at 4°C. Supernatants from all vortex washes were filtered through 70-μm mesh and pooled into 50ml conical tubes to remove villus material and tissue fragments. Isolated crypts were pelleted at 1000 rpm at 4°C. After this step, whole crypts were utilized for flow cytometry (detailed below), spheroid cell line establishment (de la Cruz Bonilla et al., 2018) and treatment (detailed below), or ChIP-seq (detailed below). For ChIP-seq, crypts were first suspended in ADMEM/F12 (D6421, Millipore Sigma)

supplemented with 10 U/mL penicillin, 10 μg/mL streptomycin, 2 mM L-glutamine, 10 mM HEPES, 10μM TGF-β RI Kinase Inhibitor VI (SB431542, Calbiochem), 10 μM Y-27632 dihydrochloride (Millipore Sigma), 0.5 mM N-acetylcysteine amide (Millipore Sigma), and 100 nM TSA. *Chromatin Immunoprecipitation.* Chromatin immunoprecipitations were performed using a previously published protocol with modifications for SI crypts (Garber et al., 2012). Briefly, whole isolated crypts from 4 animals were pooled per treatment per replicate and cross linked for 10 min at 37°C with 1% formaldehyde in supplemented media and quenched with 0.125M glycine for 5 min at 37°C. Crypts were washed with PBS with 1 × protease inhibitor cocktail (Millipore Sigma-Aldrich) and stored at −80°C. Pellets were thawed and then lysed for 30 min on ice with I-ChIP buffer (12mM Tris–HCl pH 8.0, 6mM EDTA pH 8.0, 0.1x PBS, 0.5% SDS) plus cOmplete mini protease inhibitors. Sonication conditions were optimized (60 cycles; 30 s on/off) for SI crypt cells using a Bioruptor (Diagnode) to achieve shear length of 250-500bp. 10% total chromatin was reserved as an input control. Chromatin was diluted 5 fold and immunoprecipitation was performed overnight by incubation of the sonicated cell lysate with 30 ul of protein G magnetic dynabeads (Invitrogen) previously coupled to target antibody for a minimum of 1h at 4°C. Immune complexes were then washed five times with cold RIPA buffer (10 mM Tris–HCl, pH 8.0, 1mM EDTA, pH 8.0, 140 mM NaCl, 1% Triton X-100, 0.1% SDS, 0.1% DOC), twice with cold high-salt RIPA buffer (10 mM Tris–HCl, pH 8.0, 1 mM EDTA, pH 8.0, 500 mM NaCl, 1% Triton X-100, 0.1% SDS, 0.1% DOC), and twice with cold LiCl buffer (10 mM Tris–HCl, pH 8.0, 1 mM EDTA, pH 8.0, 250 mM LiCl, 0.5% NP-40, 0.5% DOC). Elution and reverse cross linking was performed in 50 ul direct elution buffer (10 mM Tris–HCl, pH 8.0, 5 mM EDTA, pH 8.0, 300 mM NaCl and 0.5% SDS) with Proteinase K and RNaseA at 65°C overnight. Eluted DNA was cleaned up with solid-phase reversible immobilization (SPRI) beads (Beckman-Coulter). Antibody details are listed in the Key Resources Table. *ChIP-sequencing library preparation.* Library preparation was performed as described in Garber et al. (2012). Briefly, enzymes from New England Biolabs were used for the following library construction processes: DNA end-repair, A-base addition, adaptor ligation, U Excision, and PCR enrichment. ChIP libraries were barcoded using TruSeq DNA LT Adapters, multiplexed together, and sequencing was performed on HiSeq 2000 (Illumina) or NextSeq 500 (Illumina). *ChIP-seq data processing.* Raw fastq reads for all ChIP-seq experiments were processed using a snakemake based pipeline (Blecher-Gonen et al., 2013). Briefly, raw reads were first processed using FastQC (http://www.bioinformatics.babraham.ac.uk/projects/fastqc/) and uniquely mapped reads were aligned to the mm9 reference genome using Bowtie version 1.1.2 (Langmead et al., 2009). Duplicate reads were removed using SAMBLASTER (Faust and Hall, 2014) before compression to bam files. To directly compare fed and fasted ChIP-seq samples uniquely mapped reads for each mark were downsampled per condition to 20 million, sorted and indexed using samtools version 1.5 (Li et al., 2009). To visualize ChIP-seq libraries on the IGV genome browser, we used deepTools version 2.4.0 (Ramírez et al., 2016) to generate bigWig files by scaling the bam files to reads per kilobase per million (RPKM). Super ChIP-seq tracks were generated by merging, sorting and indexing replicate bam files using samtools and scaled to RPKM using deepTools. *Identification of ChIP-seq binding sites.* We used Model-based analysis of ChIP-seq (MACS) version 1.4.2 (Zhang et al., 2008) peak calling algorithm with a p value threshold of 1e-5 to identify H3K27ac enrichment over "input" background. Consensus replicate sites and unique fed and fasted sites for H3K27ac were identified using the concatenate, cluster and subtract tools from the Galaxy/Cistrome web based platform (Liu et al., 2011). Briefly, a consensus peak set was first generated by clustering intervals of replicate peaks that directly overlapped by a minimum of 1bp. Next, a shared peak set was generated by clustering intervals of fed consensus peaks that directly overlapped fasted consensus peaks by a minimum of 1bp. Unique peaks were then identified by subtracting the total number of peaks in each condition by the shared peak set. *Assigning binding sites to genes.* A list of Ensembl genes was obtained from the UCSC Table browser (http://genome.ucsc.edu/). Proximal promoters were defined as ± 5kb from the transcription start site (TSS) and the gene body was defined as all genic regions outside of the +5kb promoter region. Intergenic regions were defined as all regions outside of both the proximal promoter and gene body. H3K27ac peaks were assigned to genes if they overlapped the promoter by a minimum of 1bp. H3K27ac enhancers were identified defined as all sites outside of the proximal promoter.

QUANTIFICATION AND STATISTICAL ANALYSIS

Unless otherwise specified in the figure legends or Method Details, all experiments reported in this study were repeated at least three independent times. For murine organoid assays 2-4 wells per group with at least 3 different mice were analyzed. All sample number (n) of biological replicates and technical replicates, definition of center, and dispersion and precision measures can be found in the figure legends. The center values shown in box and whisker plots refer to the median while that in other graphs indicate mean. For analysis of the statistical significance of differences between groups, we used GraphPad Prism to perform nonparametric Mann–Whitney U (Wilcoxon rank-sum) test that allows two groups or conditions or treatments to be compared without making the assumption that values are normally distributed. No samples or animals were excluded from analysis. Unless otherwise specified in the figure legends, n > 3 young adult (3 to 5 months old) male and female mice were used for *in vivo* experiments. Age- and sex-matched mice were assigned to groups without randomization and sample size estimation. Studies were not conducted blind with the exception of all histological analyses.

DATA AND CODE AVAILABILITY

Datasets generated in this study are available at GEO repository: including population RNA sequencing data (GSE89568 and GSE67324), single-cell RNA-seq data (GSE112205) and CHIP-seq data (GSE134044). All relevant data supporting the findings of this study are also available from the lead contact (ohyilmaz@mit.edu) upon request.

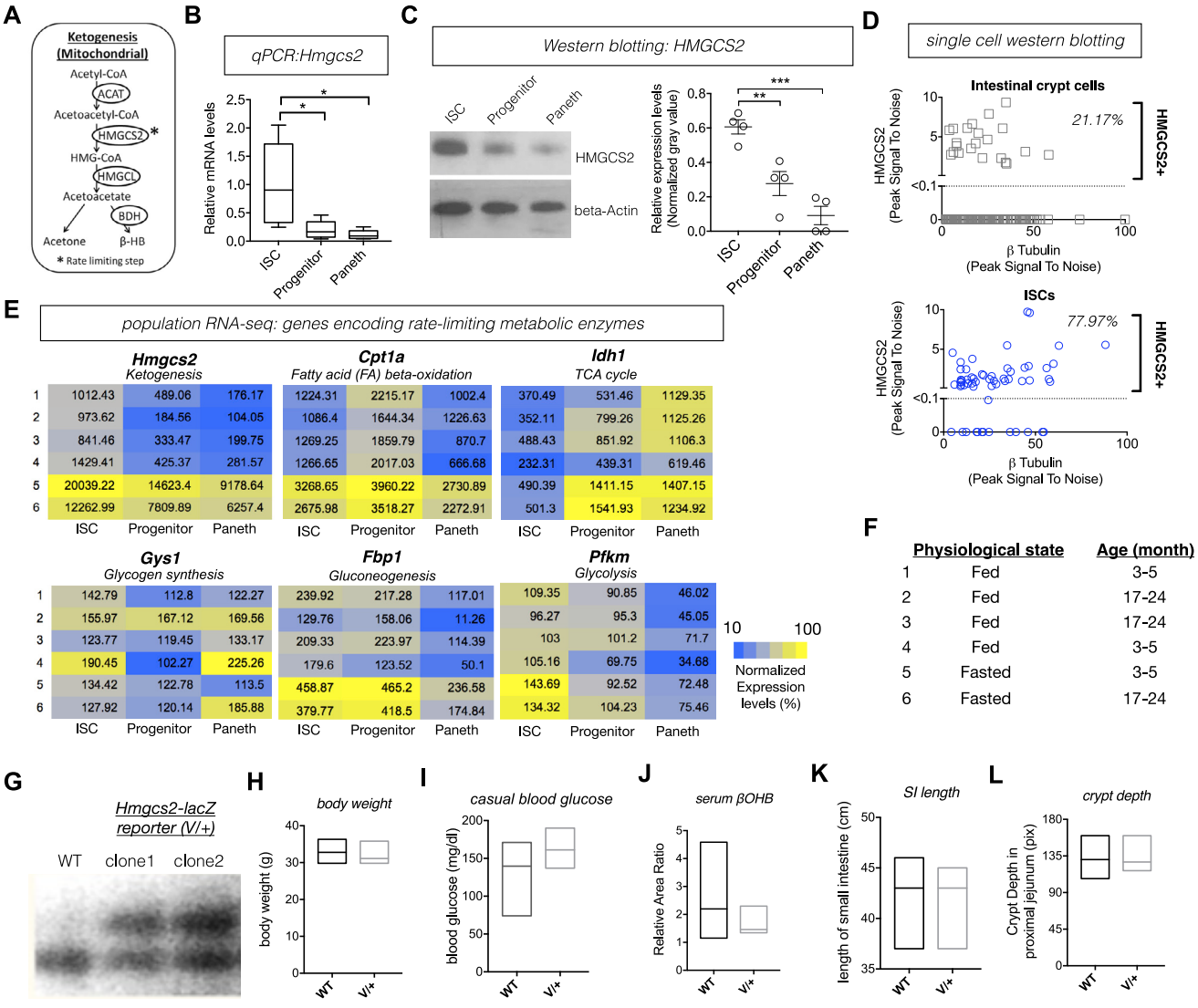


Figure S1. Characterization of *Hmgcs2* and Metabolic Gene Expression in ISCs, Related to Figure 1

(A), Schematic of enzymes involved in ketogenesis. * denotes the rate-limiting step. B, mRNA expression levels of *Hmgcs2* in flow-sorted ISCs, progenitors and Paneth cells measured by quantitative PCR (qPCR). Data were expressed as box-and-whisker 10 to 90 percentiles. *$p < 0.05$ comparing to progenitor and Paneth cells. n = 5 mice. (C), Protein expression levels of HMGCS2 in flow-sorted ISCs (*Lgr5*-GFP^{hi}), progenitors (*Lgr5*-GFP^{low}) and Paneth cells by western blotting. Relative expression levels were measured by normalized gray values of HMGCS2/beta-Actin images. **$p < 0.01$ and ***$p < 0.005$. (D), HMGCS2 protein expression in flow-sorted crypt epithelial cells (gray squares) and *Lgr5*$^{+}$ ISCs (blue circles) by single-cell western blotting. n > 250 cells per sample. (see STAR Methods for the definition and calculation of "Peak Signal to Noise"). The absolute levels of "peak signal to noise levels of HMGCS2" are not comparable across assays (chips). The cut-off (< 0.1) was set based on internal control within each assay (chip). (E), Examples of relative expression heatmap of genes encoding rate-limiting metabolic enzymes: 3-hydroxy-3-methylglutaryl-CoA synthase 2 (*Hmgcs2*) for ketogenesis, Carnitine palmitoyltransferase 1A (*Cpt1a*) for fatty acid beta-oxidation, isocitrate dehydrogenase (*Idh1*) for TCA cycle, glycogen synthase (*Gys1*) for glycogen synthesis, fructose-1,6,biphosphatase (*Fbp1*) for gluconeogenesis, phosphofructokinase-1 (*Pfkm*) for glycolysis (Rognstad, 1979; Zhao et al., 2009). See (F) for the physiological conditions and age of mice from 6 independent experiments for Sample #1-#6. (See Data and Code Availability) n = 6 mice. (G), Southern blot analysis to screen for *Hmgcs2* heterozygous-KO (*Hmgcs2*$^{v/+}$) ES clones. The WT allele (lane 1) gave a band of 9-kb, while the *Hmgcs2*$^{v/+}$ allele (lane 2 and 3) gave a 9- and a 12-kb bands. Image is representative of 25 clones. H-I, Compared to WT mice, *Hmgcs2*$^{v/+}$ mice showed no difference in body mass (H), non-fasting blood glucose levels from tail-tip sample (I), serum βOHB levels based on LC/MS metabolomics analysis (J), small intestine length (K) and crypt depth in the jejunum (L), n > 5 mice per group. Approximate Age: 3-6 months.

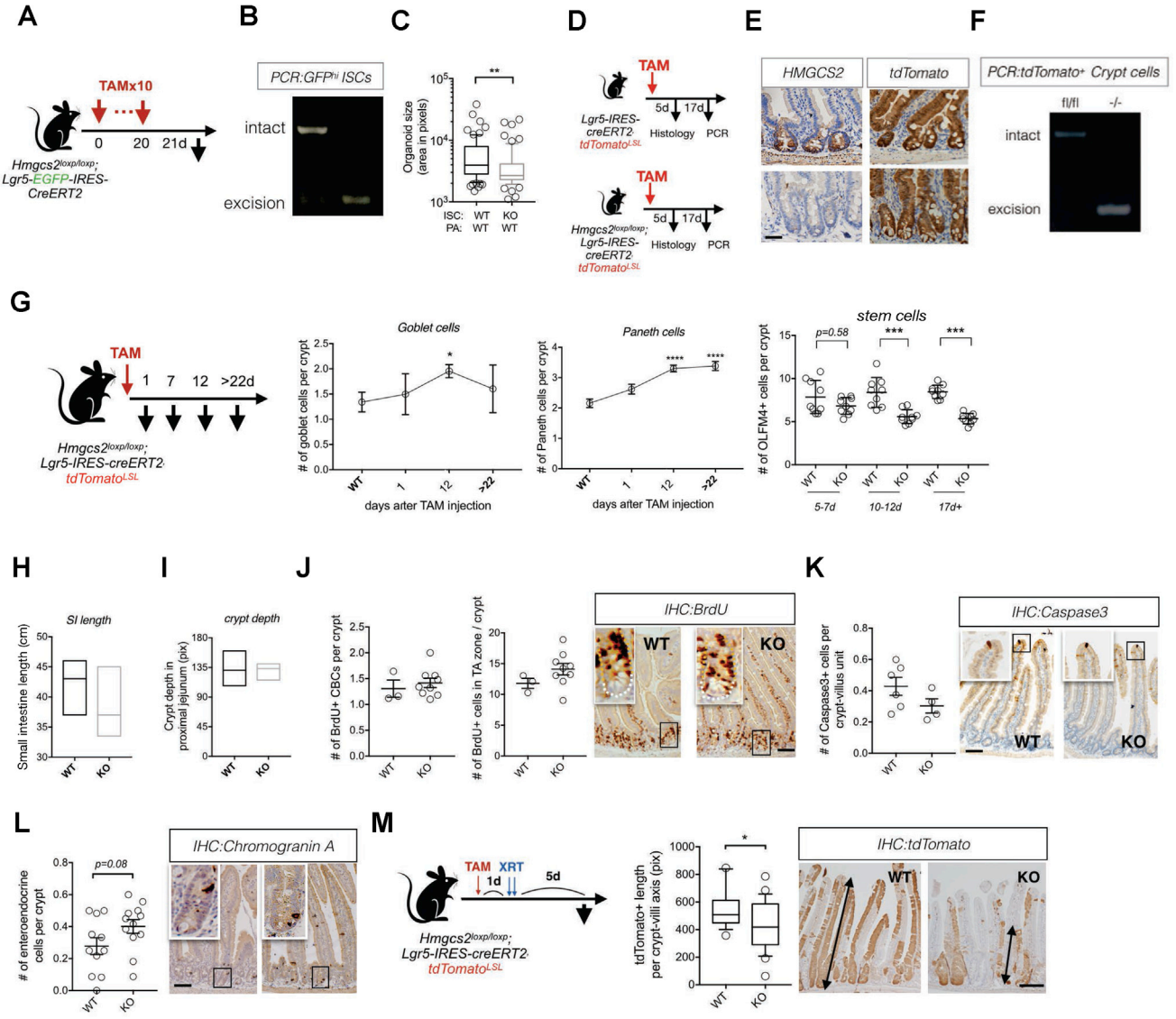


Figure S2. *Hmgcs2* Loss Perturbs Stemness and Differentiation in the Intestine, Related to Figure 2

(A), Schematic of the mouse model with the timeline for tamoxifen (TAM) injections and tissue collection. (B), Excision confirmation by PCR. WT band: 1392 bp; excision band: 408bp; Floxed band (239 bp) was not detectable (See Table S4 for primer sequences). Image represents n > 5 mice per group. (C), Organoid area from ISCs co-cultured with Paneth cells at day 5. (D), Schematic of the mouse model with the timeline for TAM injections and tissue collection. (E), IHC for HMGCS2 and tdTomato (F), Excision confirmation by PCR after TAM at indicated time. Images represent one of 5 biological replicates per group. (G), Schematic of the mouse model including the timeline for TAM injection and tissue collection. 1, 7, 12 and 17 days after a single TAM injection, small intestine tissues were collected for histology. Quantification of OLFM4^{+} cells in proximal jejunal crypts by IHC. n > 25 crypts per measurement, n > 3 measurements per mouse and n > 5 mice per group. Numbers of LYSOZYME+ (LYZ+) Paneth cells in proximal jejunal crypts by IHC, MUCIN^{+} goblet cells in proximal jejunal crypts by Alcian Blue (AB) and Periodic Acid Schiff's (PAS) staining. n > 25 crypts per measurement, n > 3 measurements per mouse and n > 5 mice per group. For (H-L), Compared to WT intestines, *Hmgcs2* null intestines have no difference in (H), length of intestine; (I), crypt depth in jejunum; (J), BrdU^{+} ISCs and progenitors, 4 hours after BrdU administration; (K), Caspase 3^{+} apoptotic cells per crypt-villus unit; (L), Chromogranin A^{+} enteroendocrine cells per proximal jejunal crypts, 17 days after TAM injection. (M), Schematic of the mouse model with timeline of TAM injection, irradiation (XRT, 7.5Gy x 2) and tissue collection. Quantification and representative images of tdTomato^{+} progeny derived from *Lgr5*$^{+}$ ISCs assessed by IHC. For box-and-whisker plots (C,F,G and L), the data are expressed as 10 to 90 percentiles. Data in dot plots are expressed as mean+/−s.e.m. Scale bars: 100um. n > 5 mice per group. Approximate Age: 3-6 months.

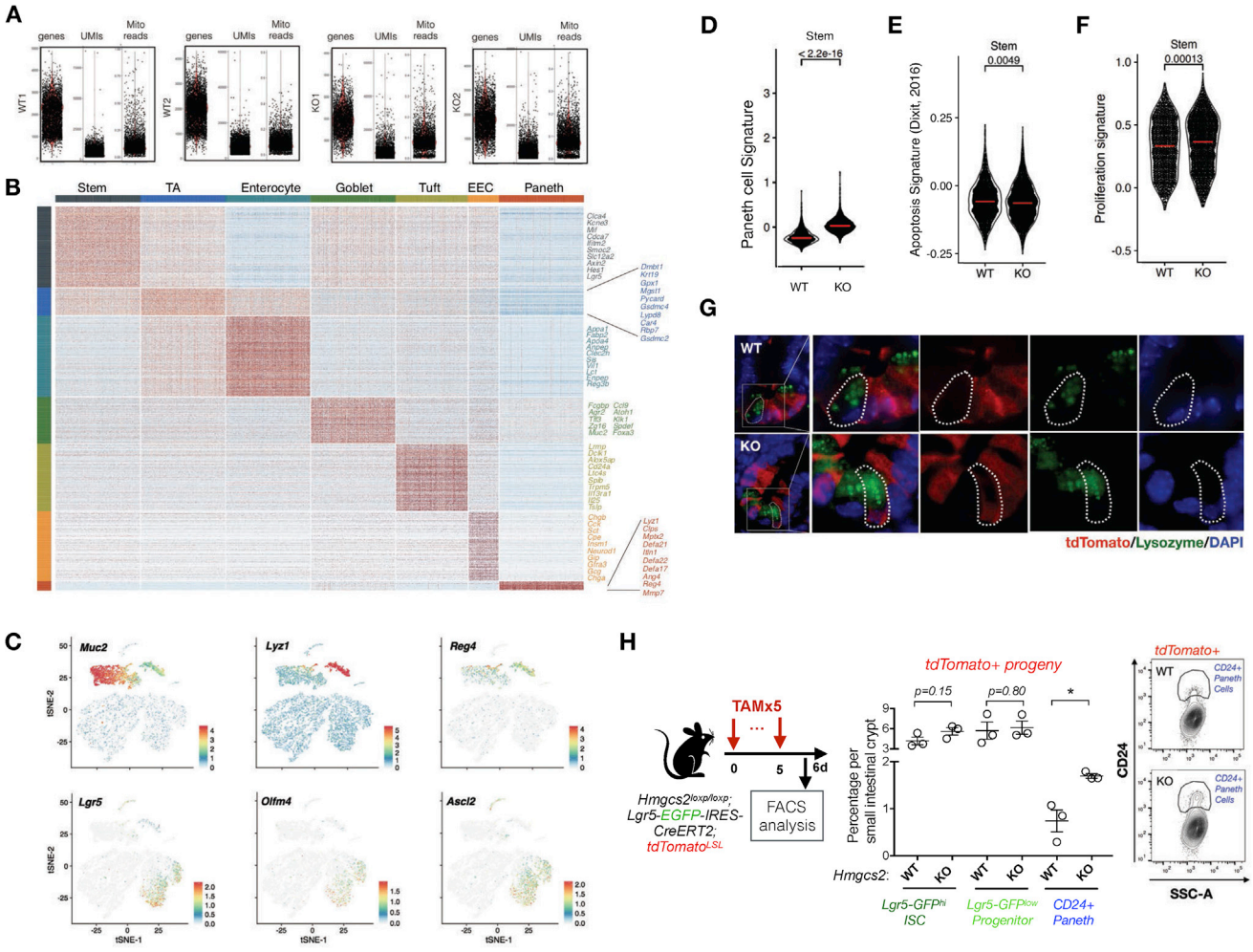
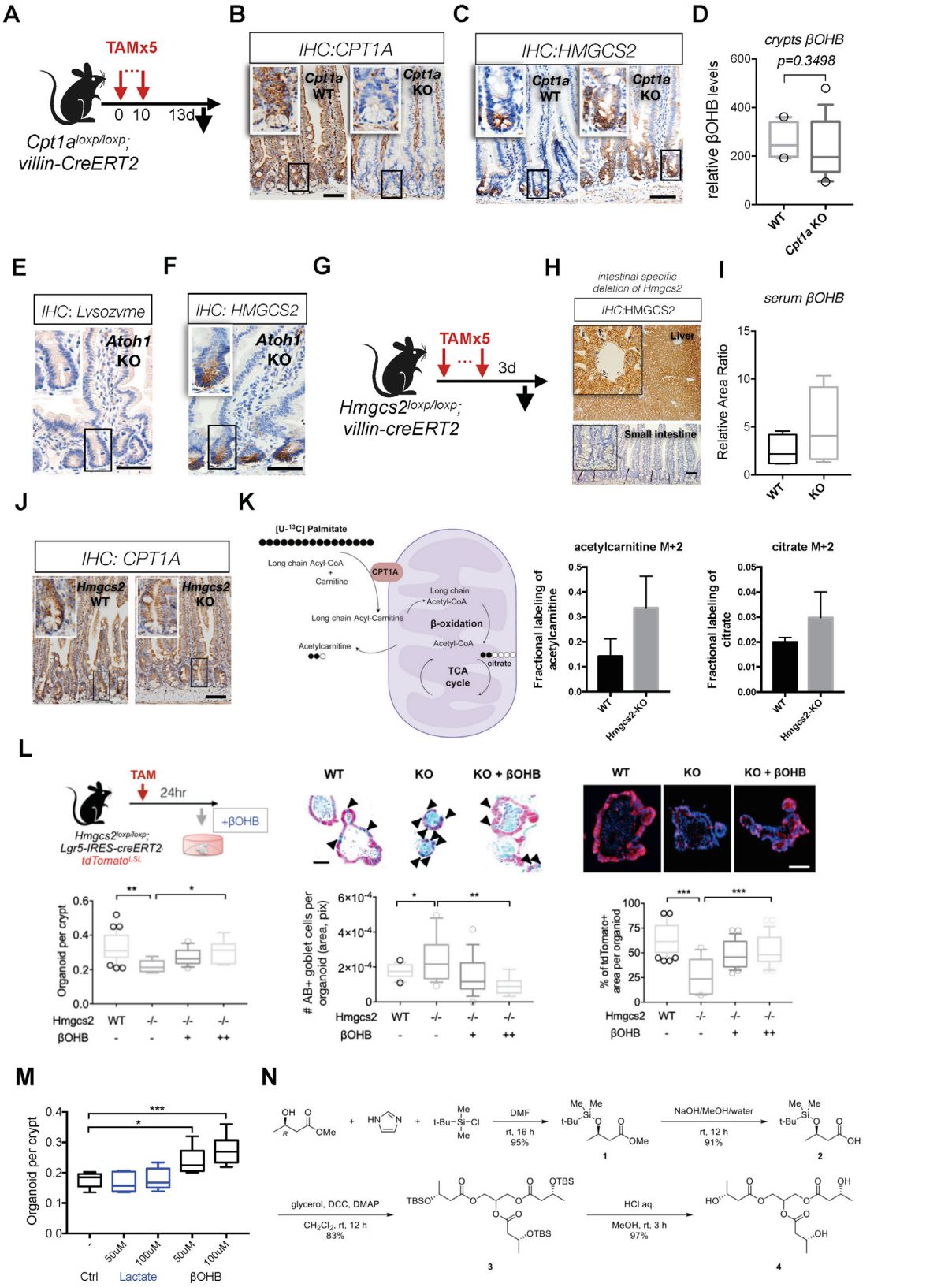


Figure S3. Single-Cell RNA-Seq Analysis of WT and *Hmgcs2* KO ISCs and Early Progeny, Related to Figure 3

(A), QC metrics (STAR Methods) and (B), Cell-type signatures. The relative expression level (row-wise Z score of log2(TPM+1), where TPM denotes transcripts per million; color scale) of genes (rows) across cells (columns) is shown, sorted by type (STAR Methods). (C), Feature heatmaps for genes encoding secretory lineage markers: *Muc2*, Mucin2, oligomeric Mucus/Gel-Forming; *Lyz1*, lysozyme1; *Reg4*, regenerating Family Member 4; and that of stem cell markers: Leucine-rich repeat-containing G-protein coupled receptor 5 (*Lgr5*), Olfactomedin 4 (*Olfm4*) and Achaete-Scute Family bHLH Transcription Factor 2 (*Ascl2*). D-F, Violin plots for mean expression of feature genes of (D) Paneth cell signature, (E) apoptosis and (F) proliferation in WT versus *Hmgcs2*-KO stem cell clusters. (G), Split channel images of immunofluorescence (IF) staining: tdTomato^{+} for *Lgr5*$^{+}$ ISCs progeny and Lysozyme (LYZ) as Paneth cell marker. (H), Schematic (left) of the mouse model with timeline of TAM injection and tissue collection for FACS analysis. 6 day after last TAM injection, intestinal crypts were isolated from mice and the tdTomato^{+} progeny of WT and *Hmgcs2*-KO ISCs were analyzed using flow cytometry (right). Frequency of *Lgr5*-GFP^{hi} ISCs, *Lgr5*-GFP^{low} progenitors and CD24+c-Kit+ Paneth cells in tdTomato^{+} crypt cells were quantified by flow cytometry.



(legend on next page)

Figure S4. Characterization of FAO and Ketogenesis in Intestinal Crypts, Related to Figure 4

(A), Schematic of the mouse model for intestinal *Cpt1a* deletion with the timeline for tamoxifen (TAM) injections and tissue collection. (B), Immunohistochemistry (IHC) for CPT1a (rate limiting step of FAO) and (C), HMGCS2 levels in WT and intestinal *Cpt1a* loss. Images represent one of 5 biological replicates per group. (D), βOHB levels in *Cpt1a* null intestinal crypts. n = 8 measurements for 4 mice per group. (E), IHC for Lysozyme, demonstrating the absence of LYZ+ Paneth cell in *Atoh1*-KO mice. The image represents one of 8 biological replicates. (F), IHC for HMGCS2, indicating intact HMGCS2 expression in the absence of Paneth cell. The image represents one of 8 biological replicates. For C-F, Scale bar: 50um. (G), Schematic of the mouse model for intestinal *Hmgcs2* deletion with the timeline for TAM injections and tissue collection. (H), Hepatic and intestinal HMGCS2 expression by IHC and (I), serum βOHB levels in *Hmgcs2*-KO mice. (J), Intestinal CPT1a expression in mice with conditional intestinal loss of *Hmgcs2* by IHC, Scale bar: 100um. The image represents one of 5 biological replicates. (K), Loss of intestinal HMGCS2 resulted in no change in FAO activity based upon the contribution of [U-13C] palmitate to acetylcarnitine and citrate. n = 6 mice per group. (L), Organoid-forming assay for number of organoids per intestinal crypt, numbers of Alcian blue$^+$ goblet cells (black arrowheads) and percentage of tdTomato$^+$ area per organoid from WT and *Hmgcs2*-KO (−/−) ISCs, ± βOHB treatments: +, 10uM and ++ 50uM. Representative images: day-5-to-7 organoids. Scale bar: 50um. n = 5 mice. DAPI(blue)/tdTomato(red). (M), Lactate treatments at comparable concentrations with β-OHB did not affect the organoid-forming capacity of *Hmgcs2*-null crypts. (N), Synthesis of glycerol tri((R)-3-hydroxybutyrate). **p<0.05, **p<0.01 and ***p<0.005.*

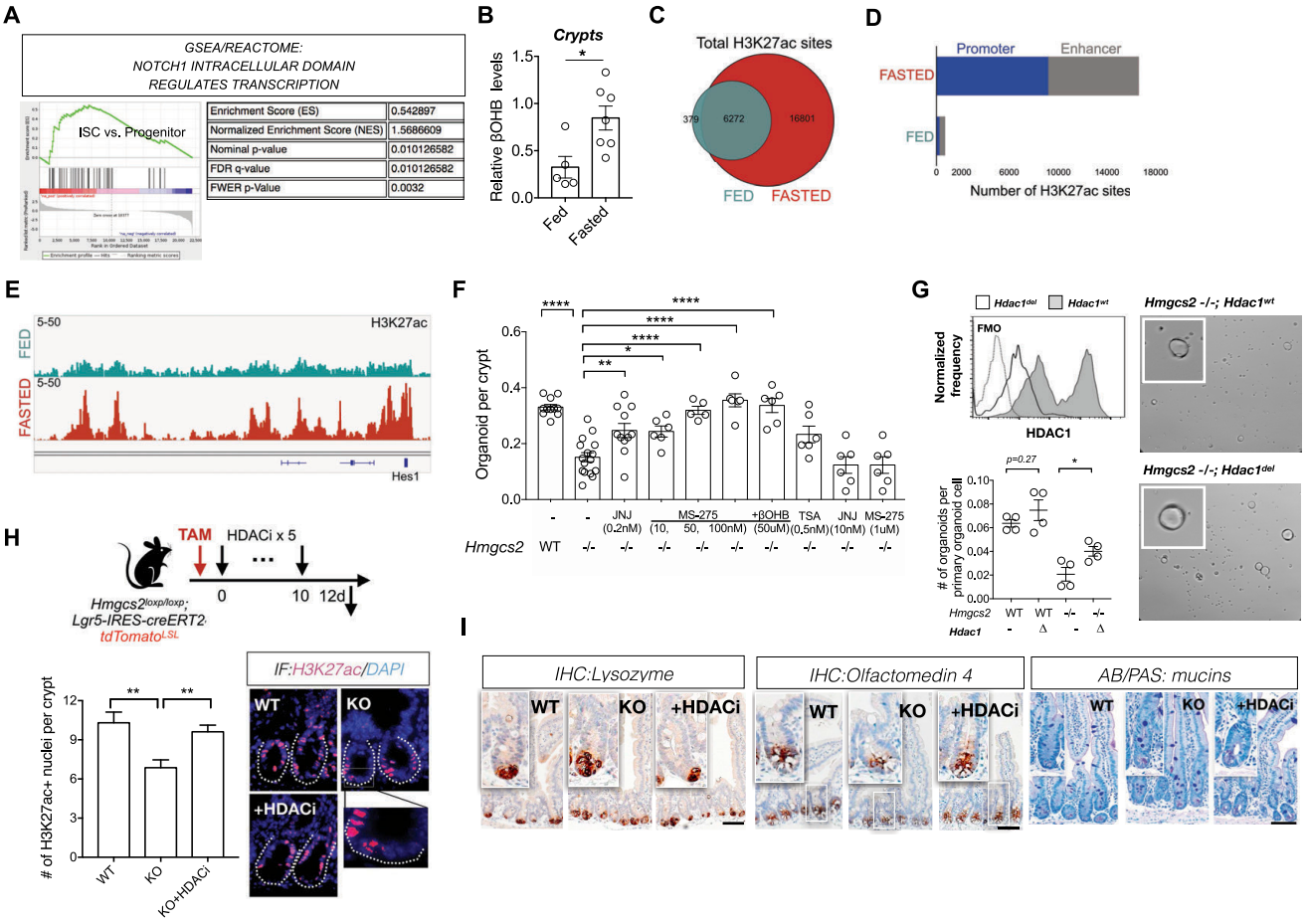


Figure S5. βOHB Regulates ISC Function via HDAC Inhibition, Related to Figure 5

(A), Enrichment plots generated by GSEA analysis for *Lgr5*-GFP^{hi} against *Lgr5*-GFP^{low}, based on gene sets from the Reactome Pathway Database (NOTCH1 Intracellular Domain Regulates Transcription). (B), βOHB levels in intestinal crypts from fed and fasted mice. Levels of βOHB were normalized to total protein of crypt cells. (C), Venn diagram analysis of lysine H3K27 acetylation (H3K27ac) sites in fed and fasted (24h) mice. (D), Barplot displaying genomic localization of H3K27ac sites in promoter (within -/+5kbTSS) and enhancer (outside -/+5kbTSS) regions in fed and fasted mice. (E), Genome browser view of ChIP-seq tracks for H3K27ac on the Hes1 locus in fed and fasted mice. (F), Organoid-formation assay for the indicated treatments. Number of organoids per intestinal crypt quantified at 3-to-5 day. JNJ, Quisinostat (JNJ-26481585); MS-275, Entinostat (MS-275); TSA, Trichostatin A. (G), Deletion of HDAC1 assessed by flow cytometey (top) and organoid-forming assay (bottom) for genetically-engineered primary organoid cells with i) *Hmgcs2*-deletion by Cre-loxp deletion, ii) *Hdac1* deletion by CRISPR/Cas9 or both i and ii. Transfected cells were sorted based on the fluorescent markers and plated onto matrigel (STAR Methods). Organoids were quantified and imaged on day 5 (n = 4 measurements from 2 independent experiments). Scale bars: 200 μm. (H), Schematic of the mouse model with the timeline of tamoxifen (TAM), HDACi (JNJ) injection and tissue collection. Immunofluorescence (IF) for nuclear H3K27ac in WT, *Hmgcs2*-KO and *Hmgcs2*-KO +HDACi. Data represents n > 25 crypts per measurement, n > 3 measurements per mouse and n > 3 mice per group. (I), Representative images of OLFM4^{+} stem cells, LYZ+ Paneth cells and AB/PAS+ goblet cells in proximal jejunal crypts by immunohistochemistry (IHC). The image represents one of 5 biological replicates. Scale bar: 50 μm, Data in the bar graph (B) and (F) and dot plot (C) are expressed as mean+/−s.e.m. For (D), box-and-whisker 10 to 90 percentiles. *p < *0.05*, **p < *0.01*, ****p < *0.001*.

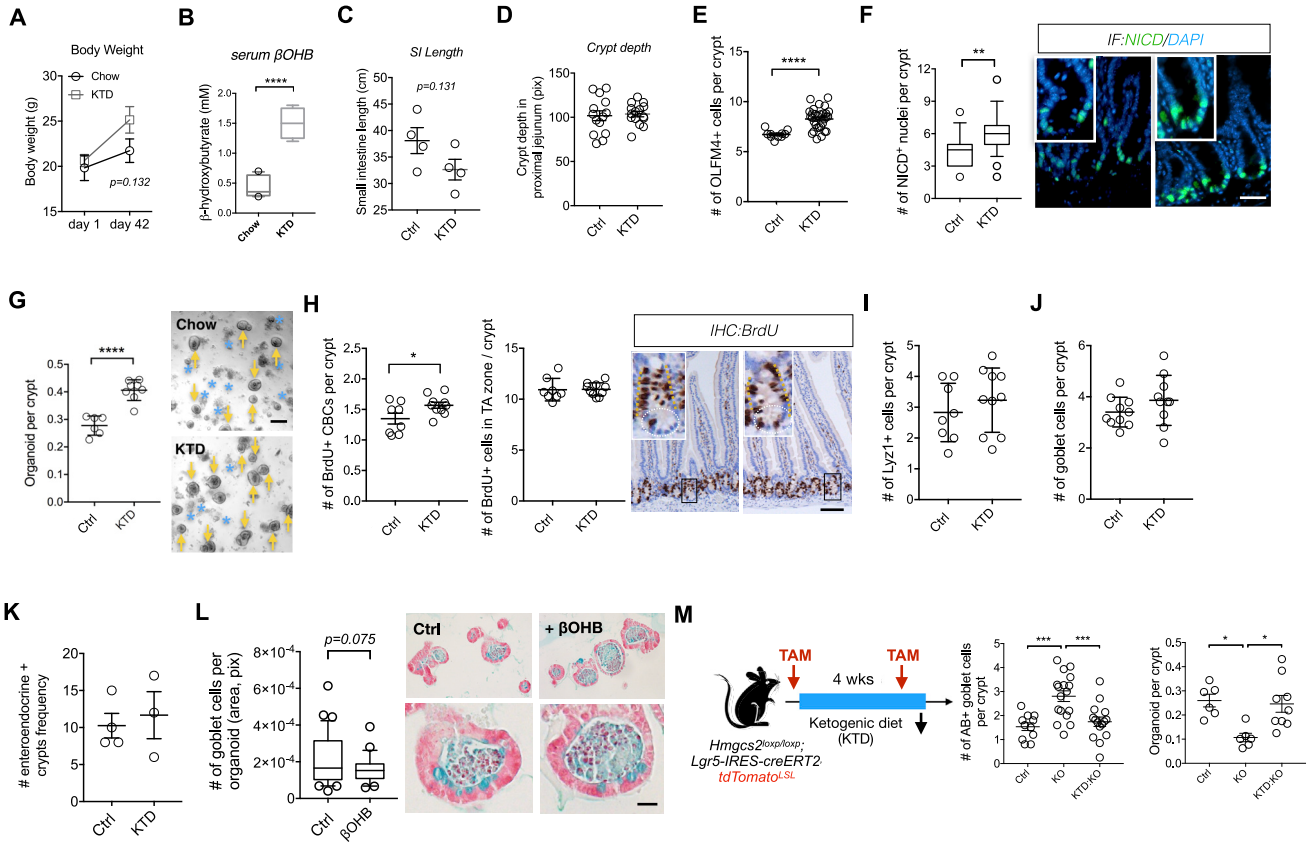


Figure S6. Characterization of the Effects of a Ketogenic Diet on ISCs and Organoids, Related to Figure 6

(A), body weight, (B), serum beta-hydroxybutyate levels, (C), small intestine length, (D), intestinal crypt depth, (E), Quantification and representative images of OLFM4^{+} cells in proximal jejunal crypts by IHC. (F), Nuclear NICD, a measure of Notch activation, by IF. Data represents n > 25 crypts per measurement, n > 3 measurements per mouse and n > 3 mice per group. G, Organoid per crypt from KTD and Ctrl mice. n = 6 mice per group. Representative images: day 3 organoids. Scale bar: 500um. For (H-K), proliferating (BrdU+) cells in the stem cell zone (CBC) and progenitor (TA) zone (H), LYZ+ Paneth cells (I), AB/PAS+ goblet cells (J), CHGA+ enteroendocrine cells (K) in the intestinal crypts were determined in mice fed a ketogenic diet (KTD) or a chow for 4-to-6 weeks (STAR Methods). L, AB+ (goblet cells) cells normalized to organoid area in wild-type (i.e., naive) organoids with or without the addition of βOHB. For box-and-whisker plots (B,F and L), the data are expressed as 10 to 90 percentiles. For dot plots, the data are expressed as mean+/−SEM *p < *0.05,* ****p < *0.001*. Scale bars for histology images: 50 μm. Data represents n > 25 crypts per measurement, n > 3 measurements per mouse and n > 3 mice per group. M, Schematic of Hmgcs2 deletion in Lgr5-IRES-creERT2 mice (Lgr5-iKO) on KTD (left). Number of AB/PAS+ goblet cells (middle) and organoid-forming capacity (right) of crypts from indicated group. WT, WT chow-fed mice. KO, *Hmgcs2* Lgr5-iKO chow-fed mice. KO:KTD. *Hmgcs2* Lgr5-iKO KTD-fed mice.

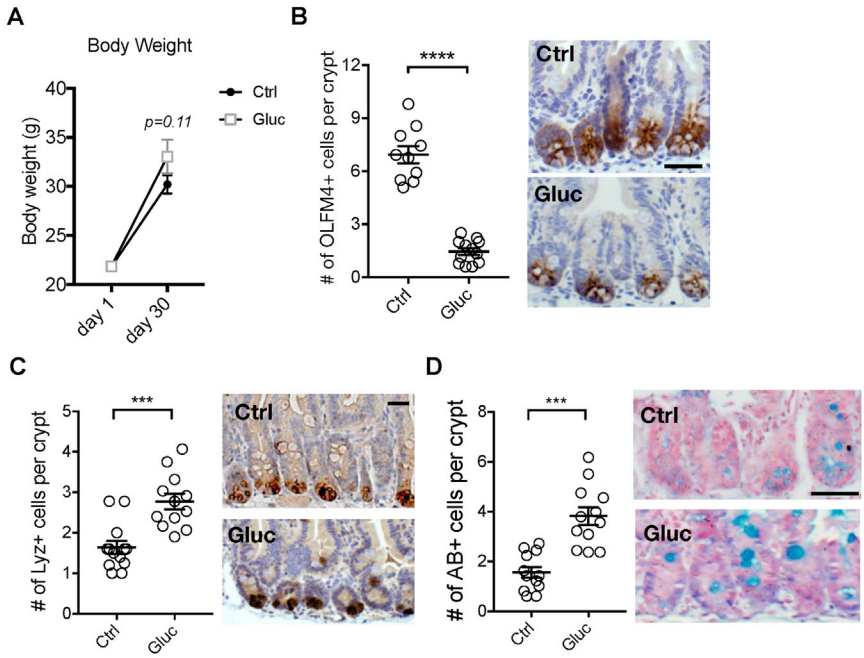


Figure S7. Characterization of the Effects of a Glucose-Supplemented Diet on ISCs and Organoids, Related to Figure 7

(A), body weight, For (B-D), Quantification and representative images of (B), OLFM4^{+} cells in proximal jejunal crypts by IHC. (C), LYSOZYME+ (LYZ+) Paneth cells in proximal jejunal crypts by IHC and (D), MUCIN^{+} goblet cells in proximal jejunal crypts by Alcian Blue (AB) and Periodic Acid Schiff's (PAS) staining. n > 25 crypts per measurement, n > 3 measurements per mouse and n > 5 mice per group. Scale bar, 50um. ****p<0.005 and ****p<0.001.*